JOURNAL OF GEOPHYSICAL RESEARCH, VOL. 111, E08008, doi:10.1029/2004JE002320, 2006

Thermophysical properties of the MER and Beagle II landing site regions on Mars

Bruce M. Jakosky,[1,2] Brian M. Hynek,[1] Shannon M. Pelkey,[1,3,4] Michael T. Mellon,[1]
Sara Martínez-Alonso,[1] Nathaniel E. Putzig,[1,2] Nate Murphy,[1,3] and Philip R. Christensen[5]

Received 12 July 2004; revised 20 March 2006; accepted 27 April 2006; published 25 August 2006.

[1] We analyzed remote-sensing observations of the Isidis Basin, Gusev Crater, and Meridiani Planum landing sites for Beagle II, MER-A Spirit, and MER-B Opportunity spacecraft, respectively. We emphasized the thermophysical properties using daytime and nighttime radiance measurements from the Mars Global Surveyor (MGS) Thermal Emission Spectrometer and Mars Odyssey Thermal Emission Imaging System (THEMIS) and thermal inertias derived from nighttime data sets. THEMIS visible images, MGS Mars Orbiter Camera (MOC) narrow-angle images, and MGS Mars Orbiter Laser Altimeter (MOLA) data are incorporated as well. Additionally, the remote-sensing data were compared with ground-truth at the MER sites. The Isidis Basin surface layer has been shaped by aeolian processes and erosion by slope winds coming off of the southern highlands and funneling through notches between massifs. In the Gusev region, surface materials of contrasting thermophysical properties have been interpreted as rocks or bedrock, duricrust, and dust deposits; these are consistent with a complex geological history dominated by volcanic and aeolian processes. At Meridiani Planum the many layers having different thermophysical and erosional properties suggest periodic deposition of differing sedimentological facies possibly related to clast size, grain orientation and packing, or mineralogy.

Citation: Jakosky, B. M., B. M. Hynek, S. M. Pelkey, M. T. Mellon, S. Martínez-Alonso, N. E. Putzig, N. Murphy, and P. R. Christensen (2006), Thermophysical properties of the MER and Beagle II landing site regions on Mars, *J. Geophys. Res.*, *111*, E08008, doi:10.1029/2004JE002320.

1. Introduction

[2] The physical properties of the Martian surface can be derived from in situ observations by landed spacecraft or from remote measurements from orbiting spacecraft. In practice, the latter can be used to understand the global distribution of surface materials, and the former to provide ground truth and to determine the nature and the range of materials that can be present at the surface. Together, they provide a compelling approach to determining the nature of the surface. An understanding of the spatial variation of the different materials at the surface and their relationship to other properties and different physical processes allows one to infer how the processes that affect the surface have operated in recent epochs. These processes, which include physical and chemical weathering of surface materials, aeolian deposition and removal, volcanism, and perhaps even fluvial deposition and erosion of materials, have played the most important role in determining the present-day surface properties. It is the surface layer that is observed by both remote-sensing and in situ measurements from an orbiter, lander, or rover, or to be sampled in a Martian sample-return mission; thus understanding these processes is key to how we interpret most other measurements that pertain to the Martian surface on a global scale.

[3] In addition, understanding the nature of the surface layer is central to our ability to select landing sites that are both safe from an engineering perspective (safely landed upon and traversed successfully by a rover) and interesting from a scientific perspective. In the extreme case, for example, landing on a surface covered by thick deposits of air fall dust is much less interesting scientifically as it would provide little opportunity to sample rocks or bedrock. Similarly, we would prefer not to land on a surface covered entirely by boulders and rocks since traversing such a surface with a rover would be extremely difficult.

[4] Our ongoing efforts have involved trying to understand the surface physical properties, how they vary over the planet, the nature of the different surface components, and the processes that might be responsible for their geographical variations. We have examined recent measurements from the Mars Global Surveyor (MGS) and Mars

---

[1] Laboratory for Atmospheric and Space Physics, University of Colorado, Boulder, Colorado, USA.

[2] Also at Department of Geological Sciences, University of Colorado, Boulder, Colorado, USA.

[3] Also at Department of Astrophysical and Planetary Sciences, University of Colorado, Boulder, Colorado, USA.

[4] Now at Department of Geological Sciences, Brown University, Providence, Rhode Island, USA.

[5] Department of Geology, Arizona State University, Tempe, Arizona, USA.

0148-0227/06/2004JE002320$09.00

Odyssey (MO) spacecraft that pertain to the vicinity of the landing sites for the Mars Exploration Rovers (Spirit and Opportunity) and the unsuccessful Mars Express Beagle II missions. These detailed analyses of specific regions complement the recent global derivations of surface properties, and allow comparison with ground truth at two additional sites (the MER sites). The present analysis follows those presented by *Golombek et al.* [2003a], *Bridges et al.* [2003], and *Christensen et al.* [2005]. Detailed comparison with the properties inferred in situ at the Spirit and Opportunity sites is included as well.

2. Data Sets Used in Analyses

[5] For this analysis, we concentrated on thermal inertia of the surface as derived from the MGS Thermal Emission Spectrometer (TES) and the MO Thermal Emission Imaging System (THEMIS). These data sets have been augmented with observations from the MGS Mars Orbiter Camera (MOC) and the THEMIS visible imager, as appropriate. Complete descriptions of the latter two data sets can be found elsewhere [*Malin and Edgett*, 2001; *Christensen et al.*, 2003] and will not be repeated here. However, we will describe the thermal inertia derivation from TES and THEMIS data, as they represent the new analysis in this work.

2.1. MGS TES Thermal Inertia

[6] Thermal inertia is derived from measurements of nighttime thermal emission from the planet's surface. For Mars, it is the major parameter that determines the diurnal variation in surface temperature, and depends most strongly on the thermal conductivity of the surface materials. It allows one to distinguish, for example, between low-conductivity dust deposits and higher-conductivity surfaces composed of rock or a cemented duricrust. More detailed descriptions of what controls thermal inertia and how results should be interpreted are given by *Mellon et al.* [2000], *Jakosky et al.* [2000], *Jakosky and Mellon* [2001], and *Christensen and Moore* [1992].

[7] Our derivation of thermal inertia from MGS TES measurements is done using the algorithm described by *Mellon et al.* [2000] and *Putzig et al.* [2005]. It involves comparison of measurements of the brightness temperature corresponding to the nighttime thermal emission measured from orbit with those predicted from a thermal model of atmospheric, surface, and subsurface temperatures. We use a radiative-conductive thermal model of the Martian atmosphere combined with a conduction model of the near-surface regolith to calculate a lookup table of bolometric brightness temperatures for a wide range of values for key physical parameters: local time of day, season, latitude, surface pressure, albedo, atmospheric dust opacity, and thermal inertia. For each observed bolometric brightness temperature we obtain values for the first six of these parameters that coincide with the observation. We use the spacecraft ephemeris to determine time of day, season, and latitude, and maps of other data sets to determine surface pressure (via topography and an assumed atmospheric scale height), albedo, and dust opacity. We then interpolate through the lookup table to obtain the thermal inertia that best reproduces the measured temperature. Additional details are described by *Mellon et al.* [2000].

[8] Total uncertainties in the derived thermal inertia were estimated to be 6% for values derived using TES bolometer data [*Mellon et al.*, 2000]. This 6% uncertainty represents a sum of estimated uncertainties from the TES measurements, thermal model, and interpolation methods used to derive thermal inertia [*Mellon et al.*, 2000]. Although thermal inertia can also be derived from spectral radiance at a particular wavelength, values derived this way are less accurate due to higher instrument uncertainty and spatially variable spectral emissivity that results from compositional or physical heterogeneity of surface materials (resulting in non-blackbody thermal emission) and from the role of atmospheric absorption by dust at some wavelengths. Bolometer-based thermal inertia is largely insensitive to these spectral effects, as they typically do not affect all wavelengths of emission. Note that the formal uncertainty in the derived thermal inertia is unrelated to our inability to uniquely derive the nature of multiple components of materials that might be present within the field of view or to the resulting interpretation. That is, it is difficult to use a single measurement to uniquely infer the abundances of multiple components (rocks, dust, duricrust, etc.). In this sense, the small uncertainty does not adequately reflect the uncertainty on the interpretation. This issue will be discussed in more detail below.

[9] A global map of thermal inertia binned at 3-km resolution (comparable to the 3 × 5.8-km resolution inherent in the observations) was created using TES bolometer nighttime data from orbits 1583–11254 (L_s 103–360° and 0–152° in the subsequent year). We employed filters on the data to eliminate observations from periods of high water-ice-cloud opacity or atmospheric dust opacity (*Putzig et al.*, 2005). The maps of TES-derived thermal inertia used here do not differ significantly from the global map by *Putzig et al.* [2005].

2.2. Mars Odyssey THEMIS Radiance and Brightness Temperature Mosaics

[10] Daytime and nighttime THEMIS data acquired through September 2003 were used to produce calibrated radiance and brightness temperature maps. Band 9 images were used (passband centered at 12.57 μm wavelength). These images were radiometrically and geometrically corrected using standard ISIS software. The georeferenced images were then mosaicked using an algorithm that adjusts the radiance of overlapping scenes by applying a linear regression [*Martínez-Alonso et al.*, 2005]. This correction is necessary because the images were acquired at different local times of day (as the orbit has changed throughout the mission) and at different seasons, and are thus subject to time of day effects on temperature and seasonal changes in atmospheric conditions. In adjusting the radiance between images, each image is matched to the brightest image in the set for a particular study area. For nighttime images, the brightest image typically coincides with the earliest local time, as temperatures decline throughout the night. This procedure effectively normalizes all of the images to the same local time, with that local time being the earliest in the scene. However, since diurnal and seasonal temperature cycles are inherently non-linear in time, this technique loses

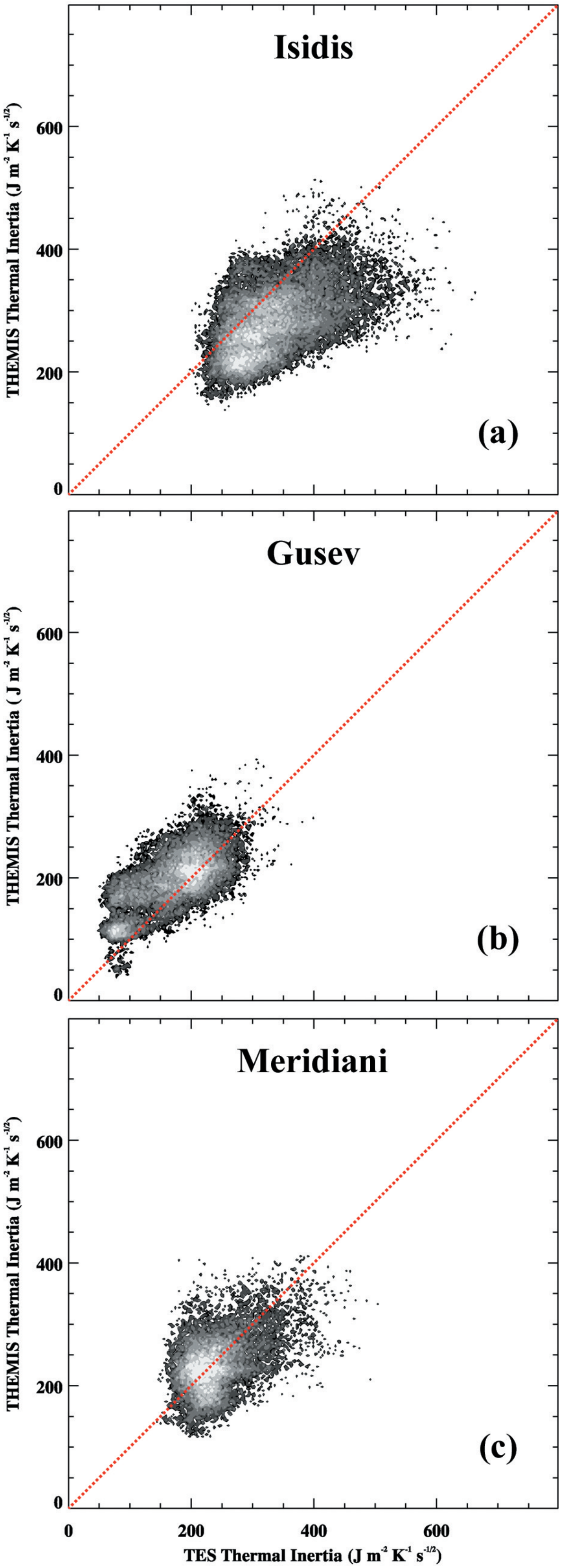

Figure 1. Comparison of TES- and THEMIS-derived thermal inertias for the three study regions discussed in this paper. For this comparison, the THEMIS data were binned to TES spatial resolution for comparison (20 pixels/degree). (a) Isidis Basin. (b) Gusev Crater. (c) Meridiani Planum.

some absolute accuracy in order to gain mosaic clarity and to facilitate ease in interpretation. The calibrated radiance mosaic was converted to a brightness temperature mosaic via a look-up table [see *Christensen et al.*, 2003]. The resulting maps have 100-m resolution, and coverage is largely continuous over the regions of interest.

2.3. Mars Odyssey THEMIS Thermal Inertia

[11] The THEMIS instrument obtains measurements of nighttime thermal emission in passbands centered at wavelengths between 6.8 and 14.9 μm wavelength. The higher spatial resolution from THEMIS measurements relative to TES provides key new information about the structure of the Martian surface, but at the expense of a lower signal-to-noise ratio and spectral resolution for nighttime measurements.

[12] We derive thermal inertia from THEMIS data using the same basic algorithm and thermal model as used for the TES data. The advantage of using the same algorithm for both data sets is that it avoids complicating the comparison of THEMIS and TES results by introducing model-based differences into the problem. We have modified our interpolation algorithm to use THEMIS Band 9 (12.6 μm) spectral-based temperature images along with ephemeris data from the MO spacecraft. When using these spectral-based temperature observations we compare the model-derived surface kinetic temperature to the Band 9 temperature in order to derive a thermal inertia. The model incorporates maps of Mars Orbiter Laser Altimeter (MOLA) elevation (for atmospheric pressure scaling) and TES-derived albedo, both binned to a spatial resolution of 1/20° per pixel (about 3 km at the equator). While TES-derived bolometric albedo is of low spatial resolution relative to THEMIS, it is the most-accurate albedo information available. Additionally, we extracted atmospheric dust opacities from the TES database [*Smith et al.*, 2001] in order to construct dust histories for each study region, using these to determine an average opacity value near the time of observation for each THEMIS image.

[13] Figure 1 compares the thermal inertia values derived for the three study regions (to be described below) from THEMIS with those derived from TES data. In each case, the THEMIS data were rebinned to TES spatial resolution. The THEMIS-derived thermal inertia values are generally in agreement with those from TES, nearly following the 1:1 line, but can differ typically by about 30–100 J m^{-2} K^{-1} s$^{-1/2}$ (these units will be used for thermal inertia throughout this paper). In different images, THEMIS values can be either higher or lower than TES values by this amount.

[14] The differences between TES and THEMIS thermal inertias probably result from a combination of possible causes. These include but are not limited to the following: (1) THEMIS observations have greater instrument noise than do TES measurements (noise-equivalent ΔT is a factor of 5 greater [see *Christensen et al.*, 2001, 2004a]). The nonlinear relationship between measured radiance and inferred brightness temperature, and between brightness temperature and derived thermal inertia, means that even random noise could introduce systematic biases in the derived thermal inertia. This is not thought to be a major factor, however, in that even an NEΔT of 0.5 K does not translate into a very large uncertainty in thermal inertia. (2) TES thermal inertias were derived with the bolometer data,

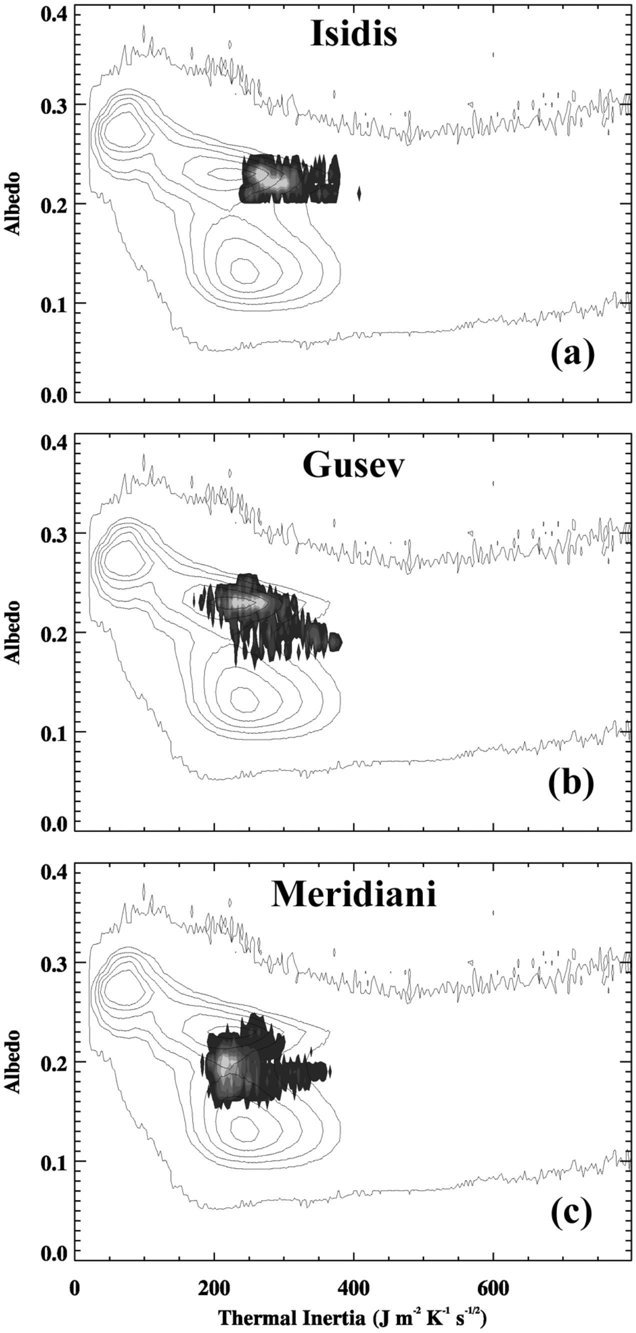

Figure 2. Two-dimensional cross plot of TES-derived thermal inertia versus albedo for the three study regions. In each case, the dark filled contours represent the points within the spacecraft landing ellipses. The light unfilled contours represent the global distribution of material properties [from *Putzig et al.*, 2005].

and THEMIS with measurements made at a particular wavelength, equivalent to using measurements from the TES spectrometer. Compositional effects on emissivity, wavelength-dependent effects derived from mixing of multiple components, and wavelength-dependent transmission and emission by airborne dust will introduce differences between the two approaches. Preliminary comparison of thermal inertias derived at the same wavelength suggests results that are more consistent with each other, as would be expected, consistent with the observed differences being a significant effect. (Note that, despite the resulting differences, we opted to utilize TES bolometer measurements instead of spectrometer measurements in our analysis. Although the comparison with THEMIS is not as good, this approach provides us with a better absolute determination of thermal inertia [see *Mellon et al.*, 2000].) (3) We use local TES dust opacity measurements [*Smith et al.*, 2001] to estimate contemporaneous dust opacity for THEMIS images whereas we assumed a uniform and constant opacity for TES. However, TES thermal inertias exhibits lower seasonal variability than do THEMIS thermal inertias, indicating that the variable dust opacity has a relatively small effect on the differences between TES and THEMIS thermal inertias. (4) The maps of topography and albedo that are used in the THEMIS analysis are at coarser spatial resolution than the THEMIS measurements, so that the THEMIS analysis may utilize inaccurate local values. (5) There may be residual alignment uncertainties between the data sets of as much as 0.15° in latitude that have not yet been corrected.

[15] All added together, we believe that the absolute uncertainty in the derived THEMIS thermal inertias is in the vicinity of 25%. Although we do not believe that the uncertainties in the measured radiance, the input parameters, and the algorithm lead to this large an uncertainty, the offset between the THEMIS- and TES-derived values, and the fact that the offset sometimes is positive and sometimes negative, suggests that there are additional factors for which we are not properly accounting. In addition, image-to-image variations can be seen in mosaics produced from multiple images, as will be discussed.

[16] As a result, our approach to interpreting the data is to use TES-derived thermal inertias as an absolute value of thermal inertia and to use THEMIS values as relative values, recognizing the differences in spatial resolution. This approach also recognizes the inherent uncertainty in interpretation of thermal inertia values caused by applying a single value to a complex surface. For mapping of Gusev, we apply a constant offset in thermal inertia to calibrate each THEMIS image to the TES map prior to mosaicking, thereby removing the bulk of the differences. In addition, we use mosaics of THEMIS nighttime brightness temperature in which many of the uncertainties associated with deriving thermal inertia from the temperature measurements do not appear.

3. Components of Materials at the Surface

[17] Although there are some absolute inferences that can be drawn from thermal inertia, we are guided to a large degree by an understanding of the types of materials that can be present at the surface. This information comes in part from analysis of data obtained at the five successful landing sites (Viking Lander 1, Viking Lander 2, Mars Pathfinder, and Mars Exploration Rovers Spirit and Opportunity, hereafter referred to as VL-1, VL-2, MPF, MER-A, and MER-B, respectively), and in part from analysis of various combinations of remote-sensing data.

[18] Figure 2 shows a two-dimensional cross plot comparing the TES-based thermal inertia and measured albedo.

This comparison allows us to put the physical properties of the study sites into the context of the global pattern, and will be of use in describing the various mechanisms affecting thermal inertia. Each panel shows data for one of the three study regions, overlaid on top of the global patterns described by *Mellon et al.* [2000] and *Putzig et al.* [2005]. The distribution generally breaks into discrete clusters. The low-inertia/high-albedo cluster is generally interpreted as deposits of air fall dust. The high-inertia/low-albedo cluster contains more-abundant rocks and duricrust. A third, cluster which lies in between the first two is intermediate in properties. These characteristics are described in more detail below.

[19] The materials identified at previous landing sites have been summarized by *Moore et al.* [1987, 1999] and integrated with remote-sensing observations by *Moore and Jakosky* [1989], *Christensen and Moore* [1992], and *Jakosky and Mellon* [2001]. For comparison in the following discussion, the current best-estimate values for thermal inertia at the first three sites were derived by *Putzig et al.* [2005] and are VL-1, 280; VL-2, 230; MPF, 390.

3.1. Unconsolidated Fine Materials

[20] All landing sites have small deposits that appear to be fine-grained unconsolidated materials. For example, one footpad at VL-1 was buried up to about 15 cm depth on landing. The VL-1 site shows drifts of material that appears to have been deposited by the wind [*Mutch et al.*, 1977], and the MPF site has small barchan dunes [*Greeley et al.*, 1999]. In addition, there appear to be deposits of dust on the leeward side of rocks and on top of individual rocks [*Mutch et al.*, 1977].

[21] The thermal conductivity of dust deposits having a particle size consistent with atmospheric air fall, less than about 20 μm, is low enough to be consistent with the lowest thermal inertias inferred for the Martian surface [e.g., *Kieffer et al.*, 1973; *Presley and Christensen*, 1997]. While extremely porous rock (such as a reticulite, an extremely porous volcanic rock) also can have low conductivity, the close association of low thermal inertia with high albedo and with regions where dust deposition is expected suggests that fine material provides the best explanation [*Palluconi and Kieffer*, 1981].

[22] Deposits of coarser grains will have higher thermal conductivity, owing to the dependence on the relationship between the pore (or particle) size and the gas mean free path and on the contribution of the gas thermal conduction to the total thermal conductivity. Thermal inertias ranging from 25 to about 400 would correspond to deposits of particles with sizes ranging from less than 20 μm up to a millimeter [*Presley and Christensen*, 1997]. Coarser grains may not have substantially higher thermal inertia, as the pore sizes are much larger than the gas mean free path and thermal conductivity becomes independent of particle size [*Jakosky*, 1986].

3.2. Rocks

[23] All five landing sites have rocks covering a portion of the surface with fractional coverages ranging from about 5 to 20% [*Moore et al.*, 1987; *Golombek et al.*, 2003a, 2005]. Rocks vary in size from centimeter-sized to larger than a meter, with the size distribution following an exponential shape with sharp drop-off at larger sizes, consistent with formation by a number of possible fragmentation processes [*Golombek et al.*, 2003a]. Few rocks are rounded and weathered, despite the potential emplacement in floods, and many have sharp edges reminiscent of fragmentation or of aeolian weathering or erosion as ventifacts. Although rocks have not been broken apart by the landers in order to access the interior, some have a solid appearance while others appear vesicular [*Binder et al.*, 1977; *Mutch et al.*, 1977]. Both MER spacecraft have observed in situ bedrock outcrops, making these surfaces unique to our collective experience.

[24] A flat, dense rock that was much larger than the diurnal thermal skin-depth (several tens of centimeters for dense rock) would have a thermal inertia of roughly 2500. Rocks that are comparable in size to (or smaller than) the skin-depth will have a larger diurnal temperature variation more similar to a flat surface having a lower thermal inertia [*Kieffer et al.*, 1977; *Golombek et al.*, 2003a]. At TES resolution, only a very small fraction of the global surface has a thermal inertia greater than 800 indicating that there are few exposures of solid rock at the several-kilometer scale [*Mellon et al.*, 2000]. THEMIS measurements show smaller exposures of apparently high thermal inertia, but no detailed quantitative analysis has been done except at a couple of sites [*Christensen et al.*, 2003; *Rogers et al.*, 2003].

[25] The abundance of rocks on the surface has been estimated from orbital thermal emission measurements. When different materials on the surface have different physical temperatures (resulting from different thermal inertias), the combined emission is non-Planckian, and the resulting variation in brightness temperature with wavelength can be used to infer the abundances of the different components [*Christensen*, 1986]. Estimated abundance of rocks varies from very low values (near zero) up to about 25%, with typical values being near 10%. These estimates have possible systematic biases, however, that result from the assumption of there being only two components of materials on the surface [*Golombek et al.*, 2003a].

3.3. Indurated Materials

[26] Materials have been identified at the landing sites that are indurated, with fine materials appearing to have been cemented together. This can be seen in the integrity of the surface where the Viking lander footpad touched down and where the rocket exhaust blew off fine material and exposed a more coherent underlying material at VL-1 [*Mutch et al.*, 1977]. Samples of this material were shaken and sieved, which disintegrated them. Several different types of indurated material, loosely termed "duricrust", were identified at the landing sites, suggesting that the degree of induration can vary from place to place locally and, by extension, globally [*Moore et al.*, 1987, 1999]. Both MER rovers conducted physical property experiments by "trenching" with their wheels [*Arvidson et al.*, 2004a, 2004b]. A duricrust surface was observed in numerous locales at the MER-A Gusev site while a coarse "lag" deposit composed the plains of the MER-B Meridiani site.

[27] Extrapolation to the global presence of duricrust has been based on remote-sensing observations. In particular,

the relatively low abundances of rocks suggests that the rock abundance observed at previous landing sites does not control the thermal inertia. Additionally, there is a lack of evidence for a surface covered in fines to match the observed thermal inertia. Measurements of radar reflectivity are best interpreted in terms of the surface porosity [see *Muhleman*, 1972], and the variation of reflectivity with thermal inertia suggests a control of both processes by the degree of formation of a duricrust [*Jakosky and Muhleman*, 1981; *Jakosky and Christensen*, 1986]. Together these analyses suggest that degree of induration of a duricrust varies spatially and is responsible for controlling thermal inertia over a substantial portion of the planet [*Christensen and Moore*, 1992].

3.4. Final Points

[28] In summary, there appear to be at least three distinct types of materials ubiquitously present at the Martian surface, as inferred from the five landing sites and via remote-sensing measurements of the global surface. These are as follows: (1) Deposits of loose, unconsolidated fine material, with varying thickness, fractional coverage of the surface, and particle size, and including possible mixtures containing different sizes. (2) Rocks of variable size, composition, vesicularity, abundance, and mechanism of origin and emplacement. (3) Cemented fines that form a duricrust, presumably with spatial variations in both the original particle size and in the degree of cementation or induration.

[29] While the thermal signature from the surface is commonly thought of as an ad hoc combination of these materials in different abundances [e.g., *Jakosky and Christensen*, 1986] it is becoming increasingly clear that geological processes have played an important role. For example, the MPF site suggests that the materials have been emplaced, sorted, and modified by the same geological processes that were responsible for the 100-m-scale geological features identified from orbit. Additionally, the surficial properties of the plains at the MER-B site are a result of differential weathering and transport of material to and from the landing site. Thus the nature of surface materials is intimately connected to the geological processes responsible for having formed or modified them, and we should expect the resulting structure of the surface to reflect a coherency and consistency among all materials [*Jakosky and Mellon*, 2001].

4. Isidis Basin (Beagle II Landing Site)

4.1. Geologic Setting

[30] The Isidis Basin is situated along the dichotomy between the southern highlands and northern lowlands. Forming the southern boundary of Isidis, the Libya Montes highland terrain is composed of Noachian cratered terrain dissected by fluvial channels terminating near the edge of Isidis Basin [*Crumpler and Tanaka*, 2003]. Material eroded from the older Libya Montes terrain may have been deposited along the southern boundary of the Isidis Basin, as fluvial fans or as the beds of paleolakes during the Hesperian period [*Crumpler and Tanaka*, 2003]. In addition to fluvial transport along the southern boundary, there is strong morphological evidence for the modification of the western rim of Isidis by Hesperian-age lava flows from Syrtis Major, which lies just to the west of the basin [*Ivanov and Head*, 2003].

[31] The floor of Isidis appears to be composed of multiple geologic units with the Hesperian-aged Vastitas Borealis Formation in the southwest floor, and an Amazonian-aged smooth plains unit extending through the central, northern, and eastern regions of the basin and believed by *Greeley and Guest* [1987] to be of aeolian and other origins. Analysis of crater densities indicates that the floor of Isidis has undergone one or more major resurfacing events, which may include a series of depositional and erosional events [*Grizzaffi and Schultz*, 1989]. The Isidis plains may have formed by the collapse of the western wall of Isidis and volcanic infilling by flows from Syrtis Major [*Tanaka et al.*, 2000], by the deposition of ocean sediments that infiltrated Isidis through the large gap in its northeastern wall [*Parker et al.*, 1989, 1993], by CO_2-vapor-supported debris flows (suggested by *Tanaka et al.* [2000]), or by volcanic flows covering the entirety of the northern lowlands [*Head et al.*, 2002]. In addition, the presence of wind streaks [*Greeley and Thompson*, 2003] suggests aeolian processes continue to be active in redistributing particulate materials within Isidis.

[32] The small-scale morphology of the central Isidis floor is dominated by Hesperian-age knobby terrain characterized by the presence of mounds that can be isolated or in arcuate formations known as thumbprint terrain [e.g., *Grizzaffi and Schultz*, 1989]. The curvilinear knobby terrain is found along the northern and western regions of the Isidis floor, while the southern edge of the floor and eastern and southeastern margins of the basin, corresponding primarily to the Amazonian smooth plains material show little to no presence of the knobby terrain. In addition, *Hiesinger and Head* [2004] identified several types of ridges using MOLA and THEMIS data. These ridges are differentiated from the curvilinear sets of knobs by their smooth morphology and sinuous appearance. *Hiesinger and Head* [2004] also note that a number of transitional ridge types exist, suggesting that a genetic link exists between the various ridge-types found within the Isidis Basin.

[33] In preparation for Beagle II's landing, *Bridges et al.* [2003] discussed the thermal inertia at the landing ellipse located near the center of Isidis Basin, based on the map of thermal inertia derived by *Mellon et al.* [2000]. They concluded that a variable mixture of duricrust, rock, and soil could explain the typical thermal inertia values of 300–400 found throughout the central region of Isidis Basin, including within the Beagle II landing ellipse. In addition, *Bridges et al.* [2003] noted the presence of lower bulk thermal inertia values (<300) to the north and west of the basin and high bulk thermal inertias (>500) along the southern boundary of the basin and partially corresponding to the Amazonian smooth plains deposit (Aps) identified by *Greeley and Guest* [1987] that lies along the southern margins and eastern half of the Isidis Basin. *Christensen et al.* [2005] analyzed THEMIS data to understand the properties in the Isidis Basin, focusing to a large extent on the high-inertia region at the southern margin. They concluded that the high thermal inertia values were unlikely to result from material transported into the basin from the highland massifs, and more likely represented a lag of high-thermal-inertia material left behind upon removal of fine

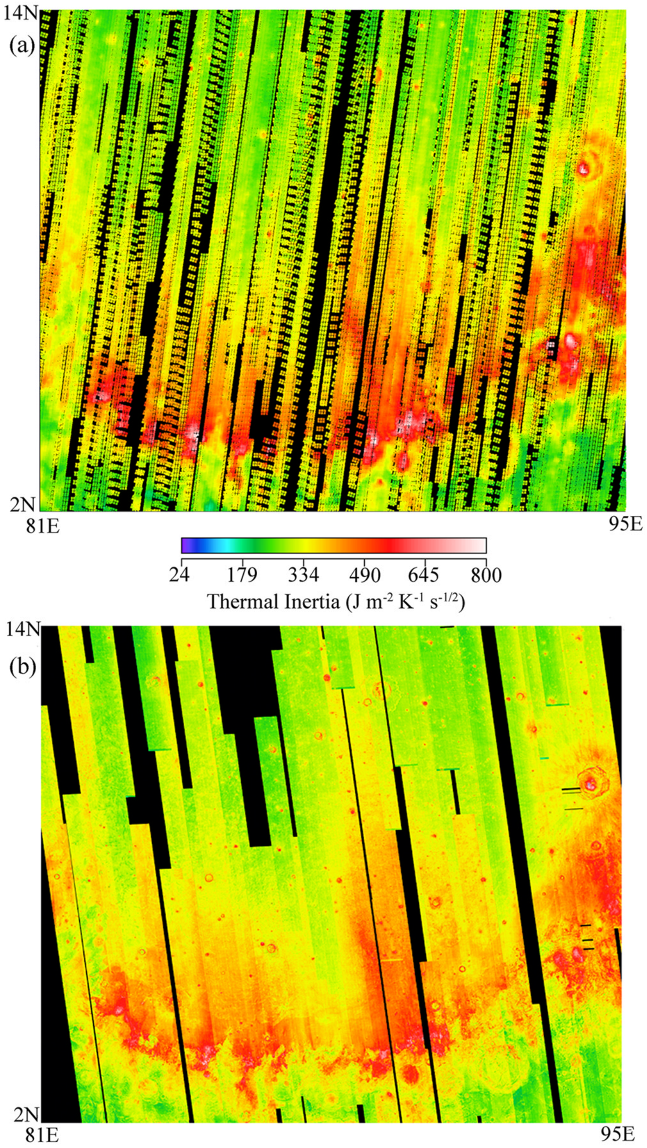

Figure 3. (a) TES-derived thermal inertia for the Isidis Basin study region. High thermal inertias exist along the southern boundary of Isidis with lobes of high thermal inertia extending to the north. (b) THEMIS-derived thermal inertia for the same region. Notice the similarity in overall structure and values.

materials by the wind. Our analysis here was carried out in parallel with that of *Christensen et al.* [2005], includes additional data analysis and comparisons with other data sets, and is complementary to their analysis.

4.2. Results and Discussion

[34] Figure 3a shows the TES-derived thermal inertia map for the Isidis study region as described in section 2.1, and Figure 3b shows the THEMIS-derived thermal inertia map for the same region. Figure 4 is the corresponding THEMIS-derived nighttime brightness temperature mosaic. Since the albedo is generally spatially uniform within the central regions of the Isidis Basin and the mosaicking technique has essentially eliminated time of day, time of year, and atmospheric effects, the THEMIS nighttime temperature corresponds closely to the thermal inertia. The gross patterns are quite similar between the two maps, with the increased resolution of THEMIS compared to TES evident when comparing Figure 3b to Figure 3a. The southern boundary of the region with higher thermal inertia and higher nighttime surface temperatures corresponds to the southern topographical boundary of Isidis Basin, shown by the shaded MOLA relief map underlying the THEMIS data in Figure 4. The terminal plains material near the massifs have TES thermal inertia values of 500–790, while the massifs themselves have much lower thermal inertias of 300–400. The high thermal inertias extend northward into the basin and then taper gradually to the lower values of the basin interior. The extension into the basin occurs most noticeably near 271°W where the high nighttime temperature and high thermal inertia extends some 300 km northward into the basin (hereafter referred to as the "thermal lobe").

[35] In order to understand the relationship between fine-scale thermal inertia and the geomorphology of the surface, we compare THEMIS-derived thermal inertia maps with THEMIS VIS images for selected locations within the dominant thermal lobe (Figures 5 and 6). The regions of highest thermal inertia near the southernmost part of the lobe, shown in Figure 5, correspond to the terminal plains unit of *Crumpler and Tanaka* [2003]. Also of note are two small hills, located in the upper central portion of the figure, showing northward low thermal inertia streaks, akin to wind streaks typically associated with craters [*Edgett*, 2002], as do some smaller features within the frame. It is unlikely

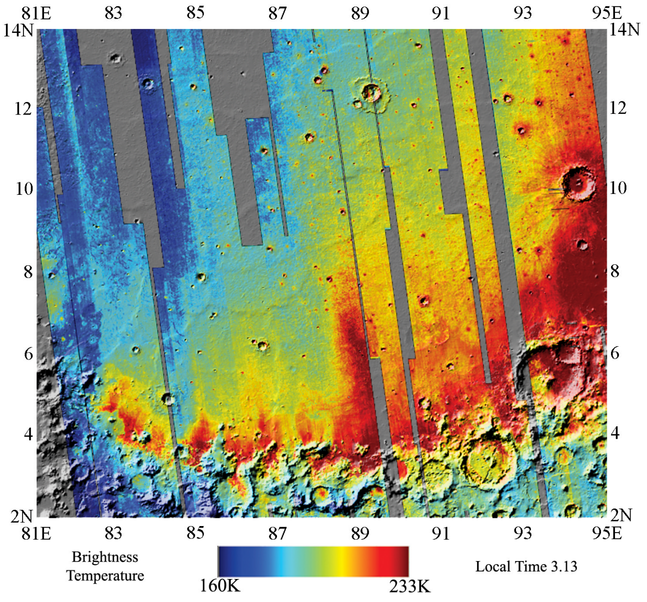

Figure 4. THEMIS nighttime brightness temperatures overlaying MOLA shaded relief for the Isidis Basin study region. As with the TES thermal inertia data in Figure 3, variations in the nighttime surface temperatures correspond to the topography along the southern boundary with high-temperature regions extending northward. The most prominent of these regions, the "thermal lobe," is clearly visible in the region 4°–7°N at 271°W.

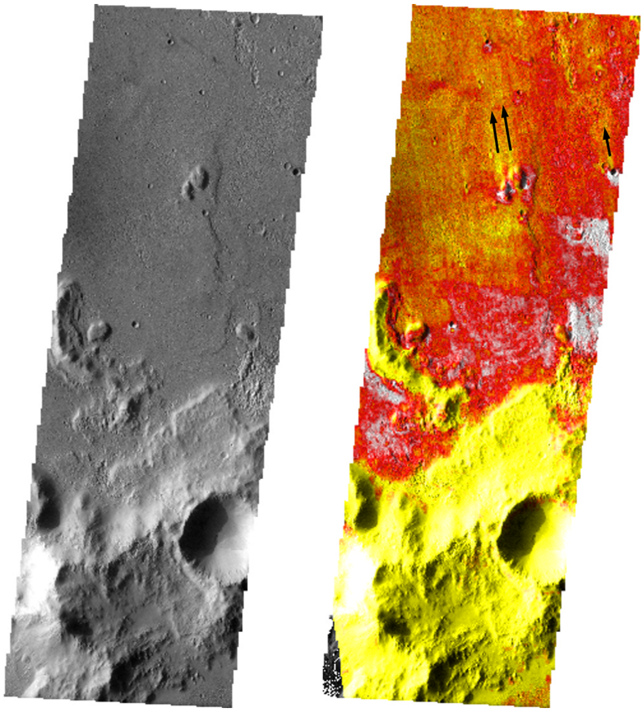

Figure 5. THEMIS VIS image V04990012 is shown on the left. On the right the THEMIS-derived thermal inertia has been overlaid on the THEMIS VIS image. These images correspond to the southern base of the "thermal lobe," which extends northward into the basin. Note the correlation between the massif and the relative thermal inertias and the presence of the northward streaks from the two small hills in the upper central area of the frame and smaller streaks associated with the small craters nearby.

these streaks are imaging artifacts because their orientation is offset from the image track by 7–9°. Figure 7 shows additional examples the thermal inertia streaks seen in the Isidis Basin, which are also unlikely to be imaging artifacts due to orientation differences up to 16° from the image track. On the basis of the lack of a matching streak pattern in the THEMIS VIS data, it appears these wind streaks do not have associated visible components, in contrast to other regions of Mars where wind streaks do show an associated albedo signature [*Pelkey et al.*, 2001; *Edgett*, 2002]. There are multiple scenarios that could result in the absence of a visible signature streak, including the presence of a dust mantle covering the entire area or the presence of materials with different thermal properties that are visibly indistinct.

[36] *Greeley and Thompson* [2003] mapped aeolian features surrounding the proposed MER Isidis landing site centered at 4.5°N and 272°W, using MOC NA images, and found wind streaks and dune orientations that strongly suggest a dominant wind direction from the west-northwest. Additionally, MOC NA image E0300958, located on the western edge of the thermal lobe, also shows wind streaks suggestive of winds from the west-northwest. These wind streak directions are in stark contrast to the thermal streaks, which show an almost exclusive south-north orientation suggestive of a dominant wind direction from the south. The large, heterogeneous vertical relief along the southern rim of the Isidis Basin may be responsible for the multiple wind-streak directions by creating turbulent wind patterns. It is also possible that diurnal or seasonal wind changes allow for the creation of wind streaks at what are nearly orthogonal orientations [*Veverka et al.*, 1981].

[37] Figure 6 shows the comparison between the THEMIS thermal inertia and corresponding VIS image at the northern edge of the primary thermal lobe. In this area, the thermal inertia has a mottled appearance with a general trend of decreasing thermal inertia toward the north. Lower thermal inertias are found within the small crater basins within the frame, indicating the crater interiors are shielded from winds scouring the surrounding smooth terrain and are also likely to serve as depositional sinks. There are no thermal wind streaks associated with the craters, which may be due to a more variable wind pattern or to a reduction in the wind intensity this far into the Isidis Basin.

[38] Also visible in Figure 6 are examples of the knobby terrain, which can be seen as small mounds within the image. The mounds are all surrounded by a ring of material with thermal inertias about 50 J m^{-2} $s^{-1/2}$ K^{-1} lower than the surrounding terrain while the knobs themselves retain a thermal inertia similar to that of the surrounding terrain. These thermal inertia rings are present in all of the observed knobs. *Hiesinger and Head* [2004] have suggested the ring is due to mass-wasting from the slopes of the knobs. The

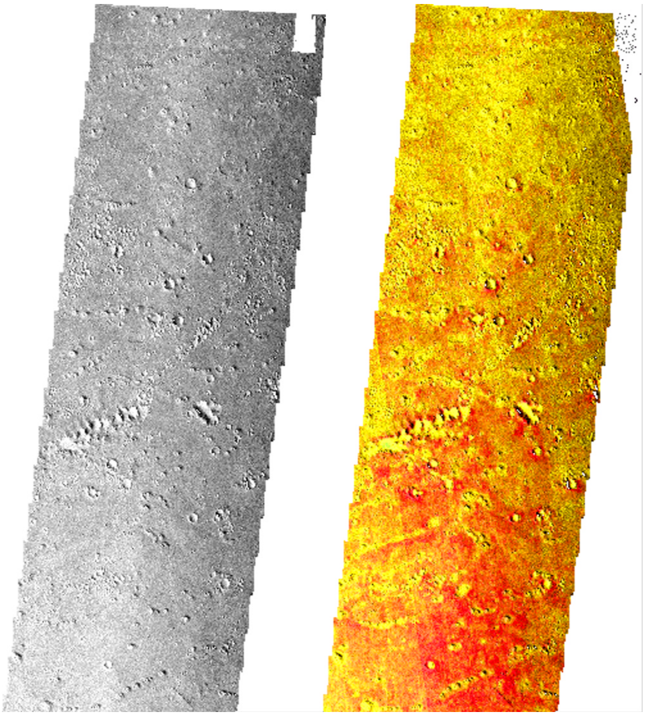

Figure 6. THEMIS VIS image V07986024 is shown on the left. On the right the THEMIS-derived thermal inertia has been overlaid on the THEMIS VIS image. This image is at the northern edge of the highest thermal inertias in the "thermal lobe." The thermal inertia has a mottled appearance due to the presence of craters, which shield their interiors from scouring, and knobs, which appear either to be resistive to scouring or to have developed after the scouring had occurred. Colors in Figures 6b and 7b have the same scale bar as Figure 3b.

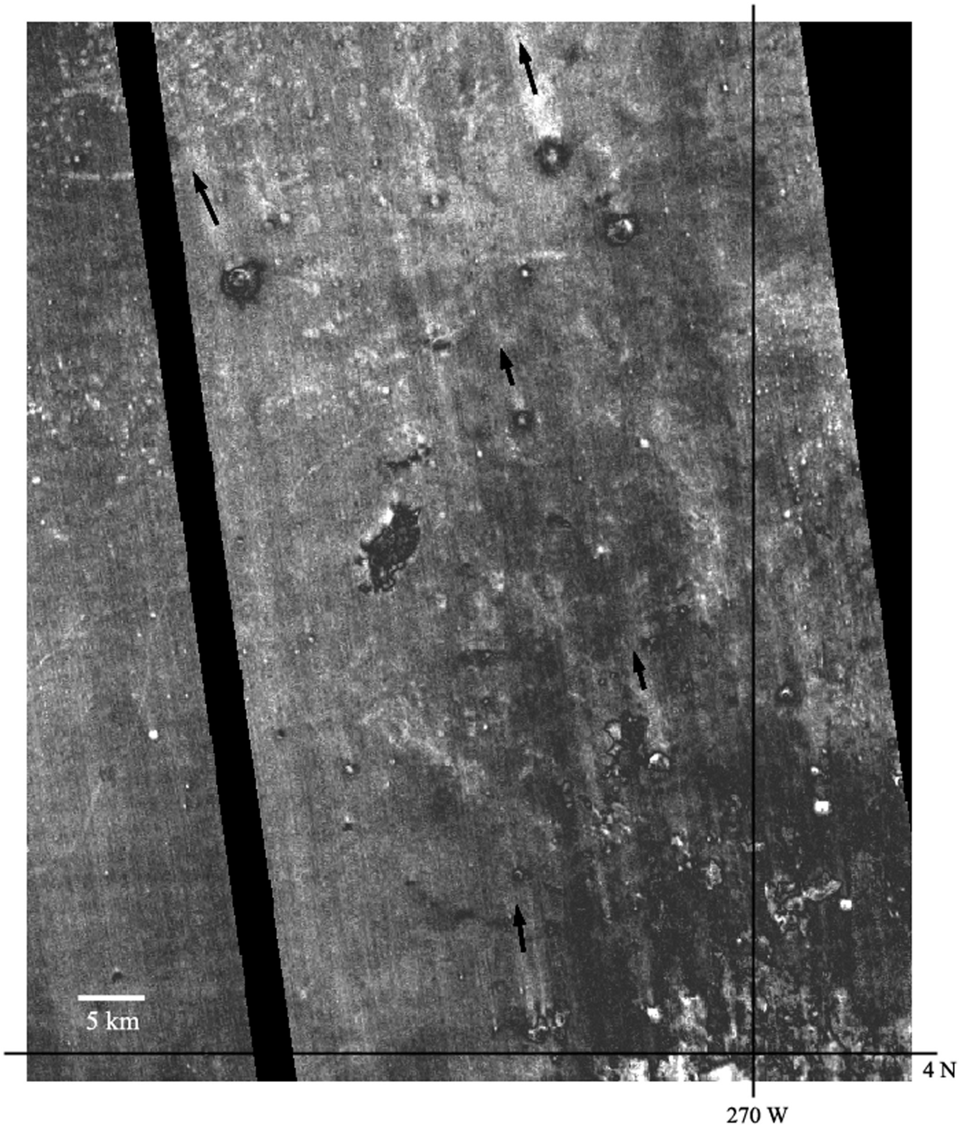

Figure 7. Wind streaks in THEMIS thermal inertia. Northward streaks, marked by the black arrows, are found throughout the high thermal inertia lobe, strongly suggesting that the high thermal inertia regions are created by scouring by winds from the south of Isidis.

thermal inertia patterns of the knobs and associated rings occur ubiquitously and thus appear to be independent of the aeolian scouring or their location within the basin. This may indicate that the ring material and knobs are more resistant to aeolian erosion than the surrounding terrain.

[39] A comparison between geologic units and the thermal inertia shows that the high thermal inertia material corresponds to the Hesperian-age fluvial deposits along the southern margin of the basin, but also extends well beyond the fluvial deposit terrain [see also *Christensen et al.*, 2005]. As stated by *Bridges et al.* [2003], there is also a partial correlation between the high thermal inertia and the Aps unit. This possible spatial correlation, however, is more likely due to the influence of the topography or other conditions of Isidis rather than to a shared history of the high thermal inertia regions and the Aps unit, due to the fact that there are areas of high thermal inertia beyond the Aps unit and areas of lower thermal inertia (values of 300–400) throughout the Aps unit.

[40] The streakiness and feathering of the large-scale thermal features and the lack of corresponding topographical, geologic unit, or morphological features suggests that aeolian activity plays a significant role in the thermal inertia patterns within Isidis [see also *Christensen et al.*, 2005]. Mesoscale modeling of the atmospheric winds in the vicinity of the Isidis Basin [*Rafkin and Michaels*, 2003] shows a daily cycle of upslope and downslope winds that is generated by the basin topography. It is possible that when the downslope winds move northward through the massifs, they are funneled through the valleys in the massifs to create a spatially variable wind pattern capable of generating the surface stress necessary to scour the uppermost surface of the basin to expose underlying higher thermal inertia material. Supporting this is the fact that the major lobes of high thermal inertia are spatially congruous with the gaps

between the massifs where the wind would likely be funneled. We suggest that the variable wind pattern may be directly responsible for the highly variable thermal inertia across the southern floor of Isidis.

[41] *Bridges et al.* [2003] hypothesized that the high thermal inertia values across the southern boundary of Isidis are due to higher rock abundances, suggesting that rocky material in Isidis was brought in from the Noachian highlands to the south of Isidis. While sediments from the highlands or elsewhere are likely the source of the material within the Isidis Basin due to the depositional history of the basin, THEMIS thermal data suggest that aeolian activity plays a significant role in altering the thermal inertia values of the surface and the thermal inertias cannot be directly linked to the depositional history of the basin. This aeolian activity may be creating thermal inertia patterns that may reflect more-recent aeolian processes rather than the depositional history of Isidis.

4.3. Conclusions

[42] The patterns of thermal inertia and nighttime temperatures derived from TES and THEMIS data suggest that the regional and local thermophysical properties are a direct result of aeolian processes within Isidis Basin, in agreement with the parallel analysis of *Christensen et al.* [2005]. The large north-trending regions with elevated thermal inertias have no topographical or visible signature in MOC or THEMIS VIS imaging, do not correlate with geologic units, and do not appear to be linked directly to debris from either Syrtis Major or the highlands to the south of Isidis. Combined with the correspondence to models of the mesoscale wind patterns, this is highly suggestive of aeolian scouring and activity within the Isidis Basin. The scouring is not uniform, suggesting that wind erosion has been highly variable within the basin. Alternatively, depositional processes may have since covered more extensively scoured regions. The thermal inertia patterns associated with the knobby terrain do not appear to be affected by the aeolian scouring, indicating a material resistant to scouring or that the knobby terrain formed after the scouring occurred.

5. Gusev Crater

5.1. Geologic Setting

[43] The interior of Gusev Crater is the landing site for the MER-A Spirit rover. Gusev is a 160-km-diameter impact crater centered at 14.5°S, 184.5°W, approximately 50 km south of the planetary dichotomy boundary. Gusev was selected as one of the two MER landing sites because of its potential for having hosted a lacustrine environment in the past [*Schneeberger*, 1989; *Cabrol et al.*, 1993, 1998; *Cabrol and Grin*, 2000; *Grin and Cabrol*, 1997; *Kuzmin et al.*, 2000]; such an environment might have been favorable for the development of biogenic activity. Ma'adim Vallis, a 900-km-long channel that debouches into Gusev, has been proposed as the conduit for water and sediments that may have filled Gusev. Drainage along this channel could either have been active over an extended period of time [*Cabrol et al.*, 1998] or have originated by catastrophic overflow of a lake located in the basin where Ma'adim Vallis originates [*Irwin et al.*, 2002].

[44] The geological units in the Gusev study area (whose upper left and lower right corner coordinates are 10°S, 190°W and 20°S, 180°W, respectively) range in age from Noachian to late Amazonian [*Kuzmin et al.*, 2000]. The southern highlands in the vicinity of Gusev consist of extensive regions of plains materials of Noachian and Hesperian age that have been heavily cratered and dissected (the "cratered plain material" units of *Kuzmin et al.* [2000]). Large Hesperian channels, such as Ma'adim Vallis and Durius Vallis, cut into this unit. The oldest unit in the region (the Noachian "mountainous material" unit of *Kuzmin et al.* [2000]) is present in discrete outcrops (e.g., Zephyria Tholus, Apollinaris Tholus) of topographically high, densely dissected materials, surrounded by plain materials. The large impact craters found in the region, such as Gusev and de Vaucouleurs, also are of Noachian age. The lowlands to the north of Gusev have been interpreted as volcanic materials erupted from Apollinaris Patera–ignimbritic materials on the northern part of the edifice, and lava flows, heavily dissected by braided channels, dominating in the southern side [*Robinson and Mouginis-Mark*, 1993], of Lower Hesperian to Lower Amazonian age [*Tanaka*, 1986]. As shown by MOLA data, chaotic/fretted terrains cut through Apollinaris Patera materials in the northwestern part of the study region and extend toward the south, occupying the floor of de Vaucouleurs Crater. Those chaotic terrains may be the result of the removal of large amounts of groundwater/ice [*Robinson and Mouginis-Mark*, 1993, and references therein] or melting of ground ice and erosion by outflows from Ma'adim Vallis and Durius Vallis [*Kuzmin et al.*, 2000]. The northeastern part of the study region is covered by Amazonian materials [*Kuzmin et al.*, 2000] interpreted as volcano-sedimentary, either ash flow tuffs [*Scott and Tanaka*, 1982] or pyroclastic or aeolian [*Greeley and Guest*, 1987]. These materials have been strongly modified by aeolian erosion, as shown by the presence of numerous, well-developed yardangs.

[45] The origin of the surface materials present in Gusev Crater is still being debated. These materials have been interpreted variously as fluvio-lacustrine, volcanic, aeolian, or a combination of all of them [*Scott et al.*, 1978; *Grin and Cabrol*, 1997; *Cabrol et al.*, 1998; *Cabrol and Grin*, 2000; *Kuzmin et al.*, 2000; *Milam et al.*, 2003; *Christensen et al.*, 2005; *Martínez-Alonso et al.*, 2005].

5.2. Results and Discussion

[46] The geomorphology of the Gusev region has been subject of study in the past by *Scott et al.* [1978], *Grin and Cabrol* [1997], *Cabrol et al.* [1998], *Cabrol and Grin* [2000], and *Kuzmin et al.* [2000]; all these studies were based on the analysis of Viking imagery. *Milam et al.* [2003], in their study of Gusev Crater's basin, utilized high-resolution visible and infrared imagery (MOC, THEMIS), MOLA elevation data, and thermophysical data (bolometric TES thermal inertia derived by *Jakosky and Mellon* [2001]), TES albedo, and THEMIS daytime and nighttime brightness temperature mosaics) to identify the geomorphological and thermophysical units present in Gusev's floor. *Christensen et al.* [2005] analyzed THEMIS data of Gusev and described depositional and erosional processes in the crater; *Martínez-Alonso et al.* [2005] studied thermophysical, spectroscopic,

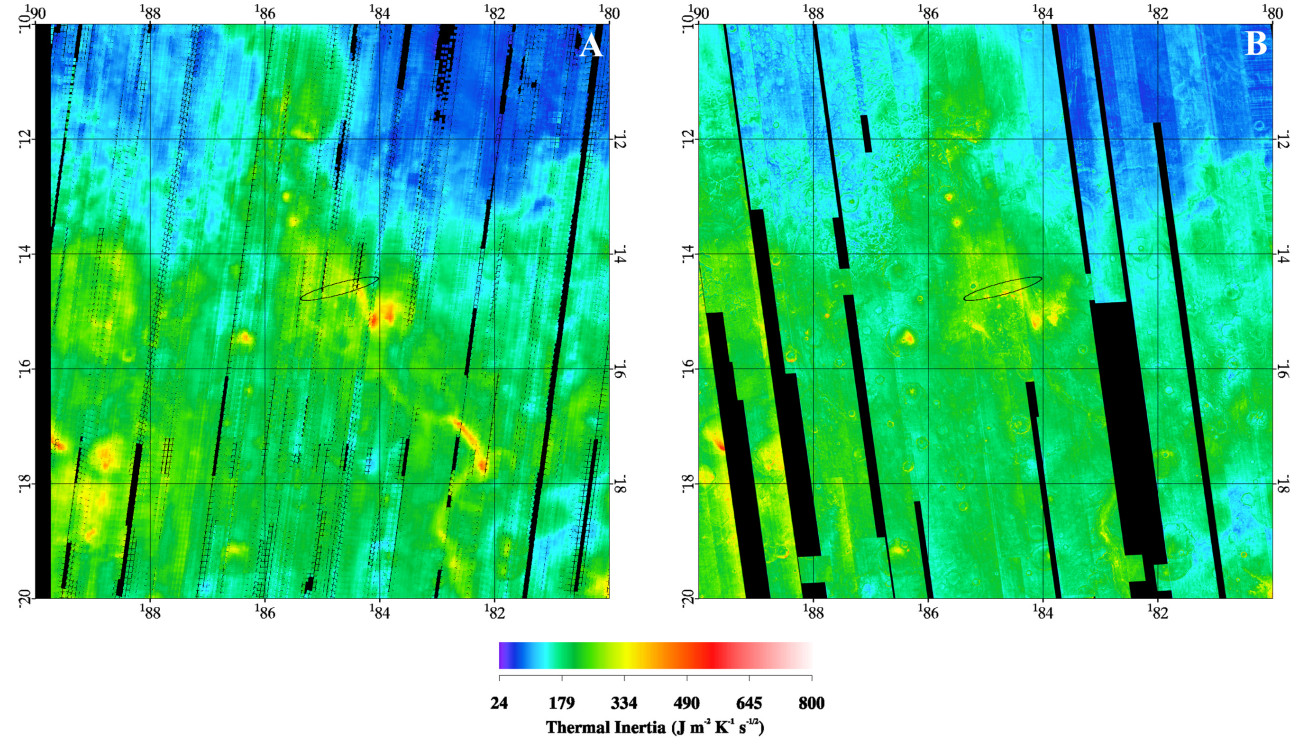

Figure 8. (a) TES-derived thermal inertia map for the Gusev study region. The MER-Spirit landing ellipse at Gusev is shown for reference. (b) THEMIS-derived thermal inertia map for the same region.

and visible data of Gusev Crater to determine the origin of its surface materials. We present results from the thermophysical analysis of newly compiled data for the Gusev region; these data include TES albedo and thermal inertia mosaics, and THEMIS radiance, brightness temperature, and thermal-inertia mosaics. Following, we describe the thermophysical units identified in this study, we contrast them with the geological units described in the previous section and with the thermophysical units described by *Milam et al.* [2003], and we discuss their significance.

[47] The TES- and THEMIS-derived thermal inertia maps for this region (Figure 8) show moderate correlation between thermophysical units and the geological units described earlier. There is a rough correspondence between lowlands and highlands, low and intermediate thermal inertia, and high and intermediate albedo, although the Apollinaris lava flows and the materials occupying the floor of de Vaucouleurs Crater have higher thermal inertia and lower albedo than the surrounding lowlands.

[48] Most of the southern highlands are occupied by the "cratered plain materials" geological unit of *Kuzmin et al.* [2000], which has intermediate TES thermal inertia values (between about 154 and 244) and intermediate albedo values (between 0.23 and 0.26). We interpret these materials as thermophysical unit Plains Materials (Figure 9), which is also present in the periphery of Gusev and in the northern and northeastern portions of that crater. The thermal inertia and albedo properties of this unit are consistent with those of an indurated surface (Figure 2; unit C of *Mellon et al.* [2000]). This unit coincides spatially with, and has equivalent TES albedo and thermal inertia values of, the WR$_t$ unit

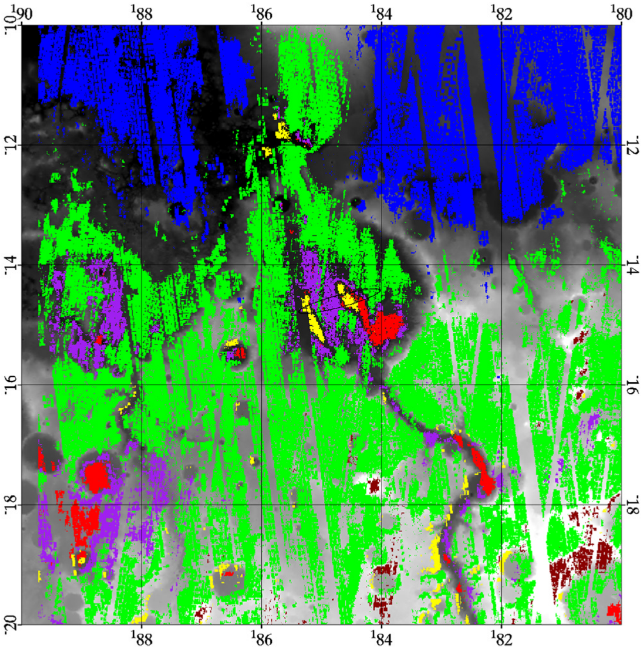

Figure 9. TES-derived thermophysical units superimposed on MOLA elevation. Green: plains materials. Brown: mountainous materials. Purple: transitional plains materials. Red: high thermal inertia. Yellow: low albedo. Blue: low thermal inertia.

of *Milam et al.* [2003], interpreted by them as a surface covered mostly in fine-grained sand.

[49] The "mountainous material" geological unit of *Kuzmin et al.* [2000] has thermal inertia values lower than the surrounding Plains Materials unit (values between 77 and 150), and low-to-intermediate albedo (between 0.21 and 0.25) (thermophysical unit Mountainous Material; see Figure 9). These thermophysical values are not unique to this unit, with some regions in the lowlands having similar values. However, this unit can be easily differentiated according to its topographic expression and geographic location. The thermal inertia values of this unit are consistent with a thick, unconsolidated dust mantle (unit A of *Mellon et al.* [2000]). Its albedo, though, is lower on average than that expected for a dust deposit, possibly due to illumination effects in the slopes of this mountainous unit. The thermal inertia of this unit corresponds to unconsolidated silt of grain size between 3 and 50 μm [*Kieffer et al.*, 1973; *Jakosky*, 1986; *Presley and Christensen*, 1997].

[50] In some locations along Ma'adim Vallis and in scattered craters in the highlands, including the southeastern portion of Gusev, a unit of high thermal inertia (values between 305 and 532) and low-intermediate albedo (0.17 to 0.26) exists (thermophysical unit High Thermal Inertia; see Figure 9). Albedo and thermal inertia values straddle over units B and C of *Mellon et al.* [2000] and unit F of *Putzig et al.* [2005], and are consistent with a surface dominated by coarse particles, exposed rocks, or bedrock (Figure 2). This unit is equivalent to the HTI_t unit of *Milam et al.* [2003] in its spatial occurrences in Gusev Crater, although our High Thermal Inertia unit also includes crater ejecta located in the northwestern section of Gusev as well as outcrops in the southwest, near Gusev's rim. *Milam et al.* [2003] interpret the HTI_t unit as very coarse sand to granule particle sizes. *Martínez-Alonso et al.* [2005] interpreted the High Thermal Inertia deposits in Gusev as materials of basaltic composition, differentiating younger lava flows and older deposits, possibly volcano-sedimentary in origin.

[51] A unit of thermal inertia and albedo intermediate between those of the Plains Materials and High Thermal Inertia thermophysical units is found in close spatial association with the latter, representing the spatial transition between those two units. This intermediate unit (thermophysical unit Transitional Plains Material; Figure 9) occupies part of the floor of de Vaucouleurs, an extensive, continuous area south of Durius Vallis, part of Ma'adim Vallis, and most of the western half of Gusev's floor. It is characterized by high thermal inertia (252 to 302), and intermediate albedo (0.23 to 0.24). This unit (corresponding to unit C of *Mellon et al.* [2000]) could consist of an indurated surface mixed with high-thermal-inertia materials, such as coarse grains, rocks, and bedrock. The Transitional Plains Materials unit coincides roughly in its spatial distribution with, and has equivalent TES albedo and thermal inertia to, the PL_t unit of *Milam et al.* [2003], interpreted by them as a surface dominated by coarse sand.

[52] A low albedo (0.16 to 0.21) and intermediate thermal inertia (127 to 369) unit (thermophysical unit Low Albedo), can be found in Gusev along two large, sub-parallel NW-SE-trending stripes, in and around Ma'adim Vallis and in some highland craters. This unit straddles between units B and C of *Mellon et al.* [2000]. It is dominated by a surface interpreted as indurated materials, coarse particles, exposed rocks, or bedrock, and is devoid of unconsolidated, high-albedo fine materials. The Low Albedo unit described here is analogous in its spatial distribution and albedo and thermal inertia values to the LA_t unit of *Milam et al.* [2003]. These authors interpret this unit as consistent with a surface of medium-grained sand.

[53] In the northern lowlands, the Apollinaris Patera volcanic materials have intermediate albedo and thermal inertia, indistinguishable from the values of the "cratered plains materials", or thermophysical unit Plains Materials. Therefore the interpretation proposed for the latter is appropriate here as well.

[54] The fretted/chaotic terrains and the materials to the west and east of Apollinaris Patera, respectively, have low thermal inertia (between 44 and 195) and high albedo (between 0.26 and 0.31) (thermophysical unit Low Thermal Inertia; Figure 9). The fretted/chaotic terrains show mesas of relatively higher thermal inertia, surrounded by troughs of lower thermal inertia. Average albedo and thermal inertia of these units are consistent with unit A of *Mellon et al.* [2000], and are characteristic of an unconsolidated, thick, dust mantle. These thermal inertia values correspond to an unconsolidated material of particle size between 1 and 150 μm [*Kieffer et al.*, 1973; *Jakosky*, 1986; *Presley and Christensen*, 1997], that is, clay-silt to fine sand.

[55] *Milam et al.* [2003] identify several thermophysical units that have no equivalent among the thermophysical units described here; they are their units MS_t, TR_t, ET_t, and MV_t. Although very distinct morphologically in THEMIS and MOC visible imagery, units MS_t (the mesas adjacent to Ma'adim's debouchment), TR_t (Thira's rim), and ET_t (Etched) were found not to differ significantly from the other units described here (i.e., the Plains Materials and Transitional Plains Materials units), either in their albedo (at TES resolution) or in their thermal properties (at TES or THEMIS spatial resolutions). Unit MV_t (Ma'adim Vallis) does not have an expression either in THEMIS or MOC visible data or in THEMIS daytime infrared data, according to *Milam et al.* [2003]. They identified the eastern boundary for this unit in THEMIS nighttime thermal infrared data. Our analysis failed to identify the proposed boundary, and found instead that the subtle variations in nighttime temperatures could be explained by small crater ejecta.

5.3. Spirit Landing Site

[56] The Spirit landing site (centered at 14.57°S, 184.53°W) has a THEMIS-derived thermal inertia value (average of the 100-m pixel closest to the landing site) of 322 (Figure 10). The TES thermal inertia for the 3 × 5-km pixel corresponding to the landing site is 300; the TES albedo for the same pixel is 0.187. Spirit's landing-site thermal inertia and albedo are representative of the Low Albedo unit described above, and therefore consistent with the properties of a surface with a mixture of indurated soil and coarse particles, exposed rocks, or bedrock, and relatively devoid of unconsolidated, high-albedo fine materials. Spirit's observations (soil characterized by mixtures of rock fragments and fine-grained particles, locally indurated) [*McSween et al.*, 2004] confirm this inference.

[57] The MER A Spirit rover landed successfully in a region of Gusev crater inferred to have undergone recent

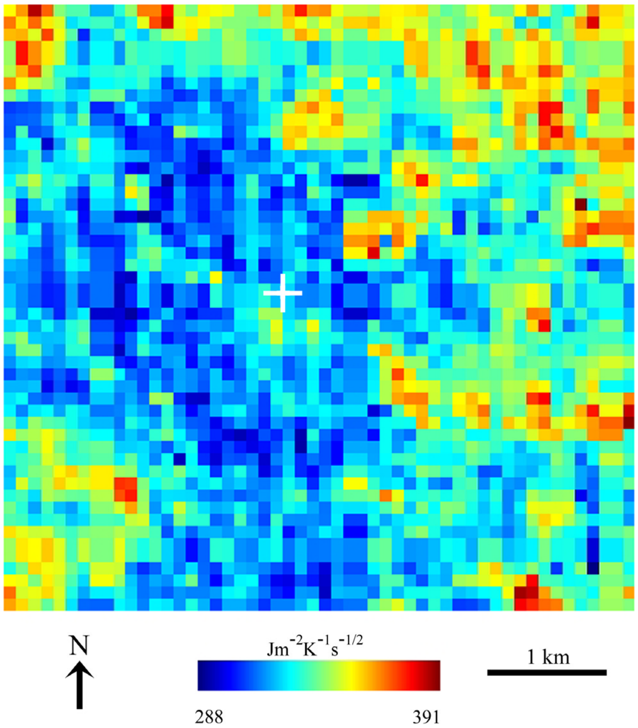

Figure 10. THEMIS-derived thermal inertias for a 5-by-5 km area approximately centered on the Spirit landing site (indicated with a white cross). Pixel size is 100 × 100 m, and north is up.

erosion of surface dust by a series of dust devils [*Squyres et al.*, 2004a]. Materials were seen both at the landing site and nearby on a series of traverses that include the same types of materials observed and inferred to be present at previous landing sites. These included deposits of windblown dust that appear to have settled out of the atmosphere, coarser-grained materials that were concentrated along the rims of aeolian ripples, materials that were cohesive either due to electrostatic forces or cementation, and rocks that ranged in size from granules to pebbles to blocks [*Arvidson et al.*, 2004a; *Herkenhoff et al.*, 2004a]. These materials are distributed in a complex three-dimensional pattern. Much of the surface appears to be coated with a thin (<1 mm) layer of dust, while other regions contain a surface monolayer of coarser grains (with two modes, 0.1–0.3 mm and 1–3 mm) [*Squyres et al.*, 2004a; *Arvidson et al.*, 2004a]. Where the surface coating is disturbed, the underlying surface often appears to be cohesive, showing a cloddy texture; the cohesion in some places goes down to the 6- to 7-cm depth excavated with the rover wheels (in Laguna hollow [*Arvidson et al.*, 2004a]). The cohesion extends down to fine scales as well, with the undisturbed soil appearing rough at sub-millimeter scales but containing individual grains smaller than the 30 μm resolution of the microscopic imager [*Herkenhoff et al.*, 2004a]. Rocks cover approximately 5% of the surface within 10 m of the landing site, with rocks larger than about 10 cm accounting for half of the total; rock abundance along the traverse of the rover varied by up to a factor of 4 [*Grant et al.*, 2004].

[58] Dust was observed to have been deposited from the atmosphere onto the rover surface and, by implication, onto the Martian surface during the primary mission [*Arvidson et al.*, 2004a]. The general absence of a thick, ubiquitous dust cover suggests that the dust is removed on a regular basis, as was observed to have occurred during the mission. This is consistent with the observed low abundance of extremely fine-grained deposits and with the general character of the surface as being one of deflation [*Greeley et al.*, 2004].

[59] The thermal inertia of individual components of the surface was determined by *Christensen et al.* [2004b] using infrared temperature measurements made from the lander and comparing them with temperatures calculated from models, in a process analogous to that carried out here. Drift material had values ranging from 300–430, while fine material filling the hollows had values between 150–240 [*Christensen et al.*, 2004b]. If these materials corresponded to loose, unconsolidated deposits of fine-grained material, the grain sizes would range from about 40 μm up to 3 mm [*Christensen et al.*, 2004b]. Some of these deposits might include grain sizes smaller than 40 μm that might be consistent with dust carried in suspension through the atmosphere.

[60] The Spirit landing site thermal inertia value of 322 determined from THEMIS data, likely arises from a combination of multiple components as observed on the surface. The interpretation of the remote-sensing data is most consistent with a surface consisting of a mixture of indurated and coarse materials. The relatively high average thermal inertia is near the upper end of the range of values derived in situ. These results suggest that the surface consists predominantly of indurated materials. While electrostatic forces can create cohesion between grains, they cannot increase the thermal conductivity. This suggests that cementation and duricrust formation are likely to be responsible for creating the cohesion.

5.4. Conclusions

[61] The geological materials present in the study area represent a large span of the history of Mars, from the Noachian to the present. The thermophysical properties of these materials are also representative of the global thermophysical units defined previously by *Mellon et al.* [2000] and *Putzig et al.* [2005]. The surface materials dominant in the northern half of the study area (coinciding approximately with the lowlands, excluding Apollinaris Patera) as well as the Noachian mountainous materials of the highlands have thermophysical properties consistent with a thick deposit of unconsolidated, fine-grained material (clay-silt to fine sand) of high albedo. The thermophysical properties of the materials covering most of the highlands, as well as these of the materials in the southern side of Apollinaris Patera and in regions of Gusev Crater, are consistent with a unit of indurated material with some rocks and/or bedrock. High-inertia materials, which could correspond to coarse grains, rocky surfaces or bedrock, are present in the floor of Gusev, in de Vaucouleurs, in a large area south of Durius Valles, and in Ma'adim Vallis.

6. Meridiani Planum

6.1. Geologic Setting

[62] One of the key discoveries from MGS has been the detection of the mineral hematite by the TES team

[*Christensen et al.*, 2000, 2001]. The hematite occurs in one primary locale, Meridiani Planum (latitude 0–3°S, longitude 352°E across the prime meridian to 1°E, covering $\sim 1 \times 10^5$ km^2). *Christensen et al.* [2000, 2001] characterized the Meridiani deposit as primarily basaltic sediments with up to 15% areal abundance of crystalline, gray, coarse-grained hematite. Most terrestrial origins of gray hematite require liquid water to be present for long periods of time, which makes Meridiani Planum an area of high astrobiological importance. This site was chosen as the landing site for the 2003 MER-B Opportunity rover [*Golombek et al.*, 2003b].

[63] The deposits within Meridiani Planum lie in a unique region of Mars that has undergone a complex history of erosion and deposition. In the Noachian epoch, extensive fluvial denudation acted to dissect and erode up to a kilometer of crust in this portion of the highlands, stretching from Margaritifer Sinus in the south up through western Arabia Terra to the north [*Hynek and Phillips*, 2001]. A thick stack of finely layered materials, including the hematite-bearing unit, was subsequently emplaced, as evident from superposition relationships with the degraded cratered terrain. The hematite-bearing unit is near the top of this ~0.5-km-thick set of layered materials. There are many layers within the complex stratigraphy, having varying thermophysical properties. Erosion has acted to differentially expose portions of the stratigraphic sequence within and around the margins of the hematite-bearing unit [*Hynek et al.*, 2002]. Abundant outliers indicate that the deposits were once far more extensive and that erosion has removed vast portions of the stratigraphic sequence.

[64] Laterally extensive plains that are smooth at all scales characterize the hematite-bearing unit. The unit (herein referred to as unit Ph) is quite dark relative to surrounding terrains and also has a low thermal inertia as derived from TES [*Arvidson et al.*, 2003]. Conversely, the group of layers immediately underlying unit Ph has been eroded into mesas, pits, buttes, and troughs, giving it an "etched" appearance (herein called unit E). Overall, these bed forms have both a high albedo and high thermal inertia [*Arvidson et al.*, 2003] and appear very bright in MOC WA and MOC NA images [see also *Christensen et al.*, 2005].

6.2. Results and Discussion

[65] Figures 11a and 11b show the regional thermal inertias derived from TES and THEMIS. Both maps have similar patterns, with the THEMIS mosaic resolving features at a much higher spatial resolution. A range of thermal inertia spanning 600 J m^{-2} K^{-1} s$^{-1/2}$ attests to the geologically diverse terrain in this region of Mars. The generalized unit contacts of Ph and E from *Hynek et al.* [2002] have been overlaid on the mosaics. Although these units were mapped on the basis of geomorphology, with no knowledge of fine-scale thermal properties, the boundaries generally correlate remarkably well with the THEMIS and TES data. Thus we interpret this region as being relatively dust-free and hypothesize that differences in thermophysical properties are a direct reflection of composition and physical properties of the morphological units.

[66] The complete hematite-bearing unit has the lowest thermal inertias in the area with an average THEMIS value of ~175, and its surface is therefore interpreted to be composed primarily of unconsolidated, fine-grained material. In stark contrast, the etched terrain typically exhibits high values with a THEMIS average of ~360. We infer that unit E contains exposures of competent rock outcrops, as previously suggested by *Edgett and Malin* [2002] on the basis of the erosional expression of the unit in MOC images and TES-derived thermal inertia and rock-abundance data. In the etched sequence, adjacent layers have thermal inertia differences of up to 80 J m^{-2} K^{-1} s$^{-1/2}$, indicative of very different thermophysical properties within the unit itself [*Hynek*, 2004]. Finer-scale layering is likely present although not resolvable in the current remote-sensing data. The etched terrain is areally extensive, and individual layered sequences can be mapped for hundreds to over a

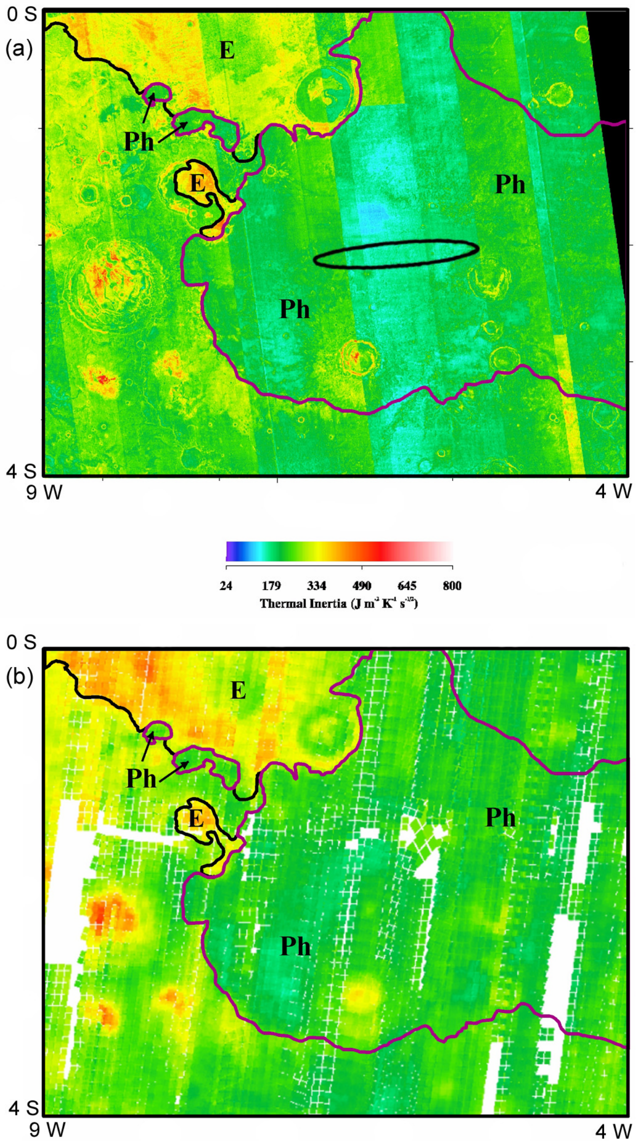

Figure 11. (a) THEMIS and (b) TES thermal inertia maps in the region surrounding the Meridiani Opportunity landing site. Unit Ph outlined in magenta is the hematite-bearing plain, and unit E refers to stratigraphically lower etched material. A large range of values is present, indicative of differing surface types.

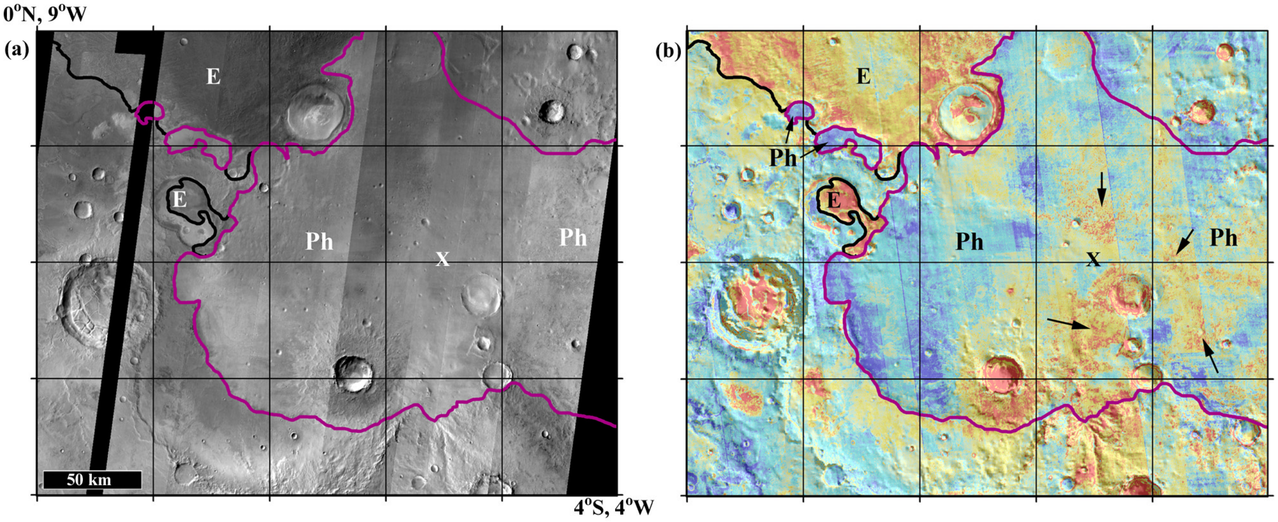

Figure 12. THEMIS (a) daytime and (b) nighttime brightness temperature mosaics of the region surrounding the Meridiani Opportunity landing site (labeled X). Unit Ph outlined in magenta is the hematite-bearing plain, and unit E refers to stratigraphically lower etched material. In Figure 12a, dark regions are cool and bright areas are warm and the range is a reflection of slope orientation, albedo, and thermal inertia. Nighttime brightness temperatures overlaid on a MOLA shaded relief map are shown in Figure 12b with a range from 177–217 K (blue-red), corresponding to a thermal inertia of ~600. Unit E is cool in the daytime and warm at night, indicating a high thermal inertia, while unit Ph is just the opposite. Mottled terrain on unit Ph is seen in the nighttime image (arrows), and we interpret these areas to contain exposures of etched material.

thousand kilometers, with most exposures north and east of the hematite unit [*Hynek et al.*, 2002; *Edgett and Malin*, 2002; *Hynek*, 2004; *Christensen and Ruff*, 2004].

[67] Figures 12a and 12b show THEMIS-derived daytime and nighttime brightness temperature mosaics of the region surrounding the Opportunity landing site (marked with an "X"). Temperatures in the daytime mosaic are a reflection of slope orientations, thermal inertia, and albedo. Nighttime temperatures are primarily controlled by the thermal inertia of the surface. The average nighttime temperature of the scene is ~70 K less than during the daytime. Abundant structure is evident in the nighttime mosaic that reflects the surface composition, grain size, and compaction (Figure 12b). The western lobe of the hematite-bearing unit exhibits some of the lowest nighttime temperatures in the region. However, over much of the extent of unit Ph in Figure 12b, discrete areas of higher nighttime temperatures are observed. At high resolution, these regions consist of fine-scale, high-brightness-temperature patches and intervening lower-temperature material. Interestingly, MOC NA images of these locations show presumably exhumed pieces of etched terrain outcropping within the hematite-rich unit [*Hynek*, 2004]. The underlying etched material is exposed as degraded and disjointed outcrops or as small mesas, ridges, and knobs that are embayed by the darker unit Ph. Areas that have a higher concentration of these inliers have a mottled appearance in both MOC and THEMIS IR data. The relatively large range of temperatures and thermal inertias in these spots likely reflect the different units.

[68] The visible and thermal infrared images also show many small craters that have "poked through" the relatively low-albedo and thermal-inertia hematite-rich unit and excavated underlying etched terrain. Light-toned, high-thermal-inertia layers are seen within the rims of craters. Large craters show this stratigraphy to depths of ~500 vertical meters; however, even craters with diameters of tens of meters show the uppermost of the layered etched terrain [*Hynek*, 2004]. The ejecta deposits of these impact craters lack a hematite signature in TES data [*Christensen et al.*, 2001]. All of these observations suggest that the layer comprising the hematite is only a fraction of the total stratigraphy and may only be a few meters thick. Further, the thickness of the subjacent etched terrain is hundreds of meters and accounts for nearly all of the positive topography associated with unit Ph.

[69] We have located the rover's landing site in our thermal inertia maps using the precise coordinates from the MER Team [*Squyres et al.*, 2004b]. Figure 13a shows the THEMIS-derived thermal inertias overlain on a 25-m resolution MOC WA and MOC NA mosaic of the region surrounding the Opportunity landing site. It is similar to the nighttime brightness temperature map (Figure 12b), and we argue that the varied thermal signatures observed correlate with the two surface types discussed above (etched terrain and hematite-rich soil). In fact, this two component surface is visible in MOC images and thermal data across the entire hematite-rich plain [*Hynek et al.*, 2002]. Expressions of etched terrain are seen both north and south of the landing site as light-toned features in the MOC images and high thermal inertia values in THEMIS data. Zooming in on roughly the navigable range of the Opportunity rover (Figure 13b; indexed by black box in Figure 13a), THEMIS thermal inertia differences of ~70 J m^{-2} K^{-1} s$^{-1/2}$ are detected in a somewhat spatially coherent pattern. Lower thermal inertia values are found to the southwest while higher values extend to the northeast. We interpret the low-

thermal-inertia region to be a result of deposition of fine-grained materials on the lee side of an unnamed crater that is centered southeast of the image at 2.3°S, 5.2°W. This light-toned crater streak is visible in MOC WA images and these depositional streaks downwind of craters have been examined in the thermal infrared previously [e.g., *Pelkey et al.*, 2001].

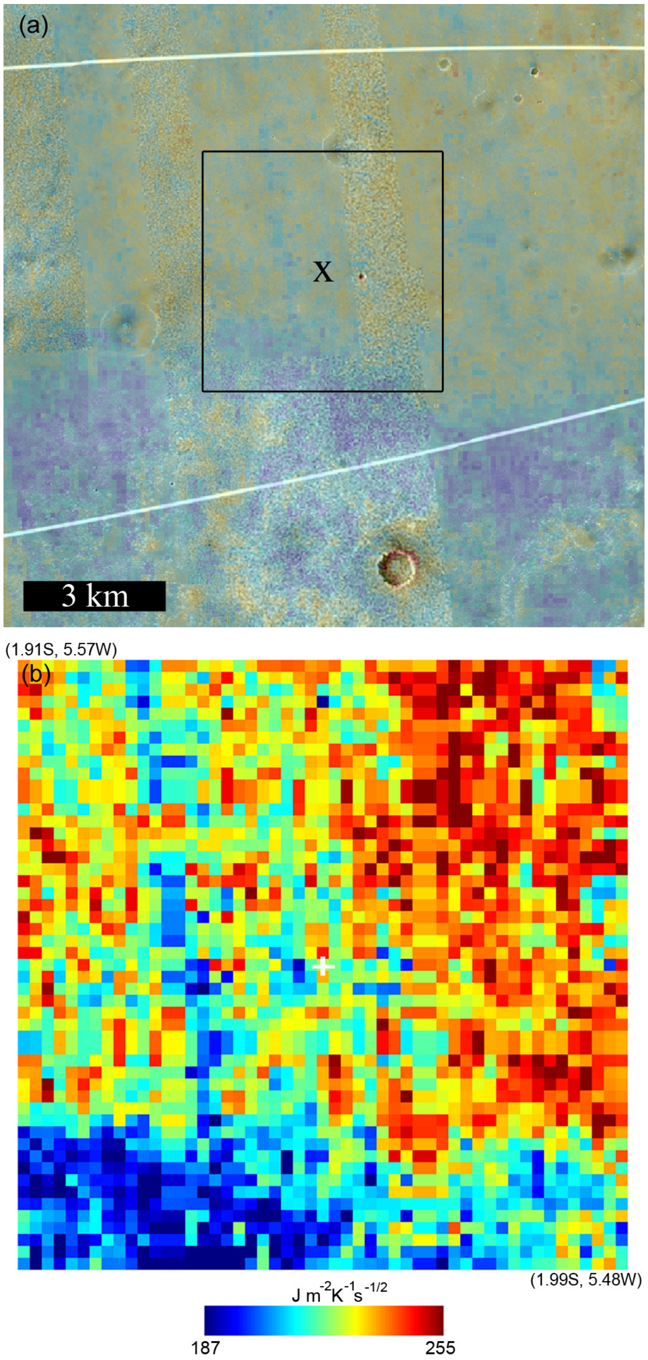

Figure 13. THEMIS thermal inertias in the vicinity of the Opportunity landing site. Figure 13a is a MOC WA and MOC NA mosaic and includes the landing ellipse (image credit: MSSS/JPL/NASA). The colors represent THEMIS-derived thermal inertia draped over this base image (180–310 for blue to red, respectively). High thermal inertia values probably represent outcrops of etched material that is similar to the bedrocks examined at the landing site. The black box shows the extent of Figure 13b, which is a zoomed in view of the approximate navigable range of the Opportunity rover (crosshairs indicate the most likely point of landing). Pixel size is 100 × 100 m in Figure 13b, and north is up in both images.

6.3. Opportunity Landing Site

[70] The THEMIS-derived thermal inertia of the 5 km box surrounding the Opportunity landing site is 220 with a standard deviation of 10 J m^{-2} K^{-1} s$^{-1/2}$ (Figure 13b). The TES thermal inertia pixel that contains the landing site has a value of 222, indicating very good agreement between the two instruments in this particular locale. The average of thermal inertias derived from the miniTES instrument aboard Opportunity itself is ~225 [*Golombek et al.*, 2005; *Fergason and Christensen*, 2005]. Thus ground observations match the remote-sensing data remarkably well. The thermal inertia values at the Opportunity site are at the low end of values for the earlier landing sites [*Putzig et al.*, 2005]. This is in part because of the very low rock abundance on the plains of Meridiani [*Golombek et al.*, 2005].

[71] Here, we combine the reported observations from the Opportunity landing site [*Squyres et al.*, 2004b; *Herkenhoff et al.*, 2004b; *Soderblom et al.*, 2004; *Arvidson et al.*, 2004b] with the local remote-sensing data (Figure 13b) to better understand the context of the Opportunity Rover and interpretation of the global THEMIS thermal inertia data. Several surface components compose terrain sampled by the Opportunity Rover. Bedrock outcrops are exposed in the walls of craters, including the 20-m-diameter Eagle Crater in which Opportunity landed. None of the craters thus far examined by the rover exhibit a well-developed ejecta blanket, and few large rocks are strewn on the surrounding plains. At least one occurrence of bedrock is not associated with an impact crater. These rocks are exposed within few-meter-long, shallow linear troughs, named the Anatolia trough system. The bedrock has been interpreted as sedimentary rocks primarily consisting of medium to coarse sand grains cemented together by an agent that is likely a combination of sulfate salts. Hematite-rich spherules, typically a few millimeters in diameter, are found within the bedrocks at roughly ten percent by volume [*Herkenhoff et al.*, 2004b; *Squyres et al.*, 2004b]. It is noteworthy that this rock is mechanically soft; the Rock Abrasion Tool on the Opportunity Rover expended 30–50 times less energy grinding this rock than while grinding basaltic rocks at the Gusev landing site and in terrestrial experiments on volcanic rocks.

[72] The second major surface component at the Opportunity site is loose, unconsolidated material that composes the soil at Meridiani Planum. This material is unlike that sampled at any previous landing sites. A thin layer of hematite-rich spherules makes up the upper section of soil in most locales. This feature has been interpreted as a lag deposit [*Squyres et al.*, 2004b; *Herkenhoff et al.*, 2004b] formed from the differential erosion of preexisting, local bedrock. Below this layer, spherules are observed in very low abundance in a matrix of unconsolidated, weakly cohesive, sand-sized and smaller basaltic grains. In general,

typical grain sizes in the soils range from 50–150 μm [*Soderblom et al.*, 2004]. Additionally, some soils have a weakly cemented duricrust that is at least 1 mm thick [*Herkenhoff et al.*, 2004b]. On the plains of Meridiani the soil has been worked into aeolian ripples, in which millimeter-sized grains armor underlying finer grained sand and dust [*Soderblom et al.*, 2004]. Soils that have been studied within crater bottoms are similar to soils on the surrounding plains.

[73] In terms of areal extent, soil dominates the coverage surrounding the landing site. Thus much of the thermal signature around Meridiani Planum is controlled by the unconsolidated matrix of grains typically 50–150 μm in size with an additional component of hematite-rich spherules a few millimeters in diameter. Laboratory experiments indicate that the matrix should have a thermal inertia of ~150–200 [*Presley and Christensen*, 1997]. A surface composed entirely of 3.5-mm-diameter unconsolidated spherules is expected to have a thermal inertia of ~410 [*Presley and Christensen*, 1997]. At sizes larger than this, thermal inertia is independent of particle size because the mean free path of the conducting gas is much smaller than the pore spaces [*Jakosky*, 1986]. Regardless, a matrix of mostly 50–150 μm particles with a minor contribution from millimeter or larger spherules should result in a thermal inertia intermediate to the two populations, which is exactly what is seen locally, where the mean value is ~220. The thermal inertia values of the soils likely reflect the duricrust component that is observed in some of the trenching experiments [*Herkenhoff et al.*, 2004b; *Arvidson et al.*, 2004b]. Bedrock around the landing site makes up only a few percent of the areal extent and therefore is only a minor influence on the thermal inertia signature. The physically weak bedrock probably has a thermal signature far below that of most competent types of rock. Indeed, where the etched terrain is seen without a soil lag to the east of the hematite-bearing plain, the thermal inertia values are 300–650 [*Hynek*, 2004], which is far less than typical bedrock values of ~1500–3000. Thus we hypothesize that the thermal inertia values surrounding the landing site are only slightly higher than in the complete absence of bedrock. Finally, the MER Team infers a relatively dust-free surface from the Opportunity observations [*Arvidson et al.*, 2004b], which was expected from the low albedo surface (mean of 0.15) for the hematite-bearing plain as determined by TES [*Arvidson et al.*, 2003].

6.4. Conclusions

[74] The hematite-bearing unit is one layer in a thick and complicated stratigraphy that is mappable for thousands of kilometers. It exhibits a low albedo and thermal inertia while underlying etched terrain has high values. Within the hematite unit, THEMIS and MOC NA images show exposures of underlying etched terrain and impacts that have excavated buried materials. A surface thermal inertia spanning ~70 J m^{-2} K^{-1} $s^{-1/2}$ within a few kilometers of the Opportunity landing site probably reflects these different units. The majority of the areal extent of terrain surrounding the landing site is composed of weakly cohesive soil that ranges in particle size from <50 μm to 6 mm as seen by the microscopic imager on Opportunity [*Herkenhoff et al.*, 2004b; *Soderblom et al.*, 2004]. The upper layer consists of a concentration of mm-sized hematite-rich spherules with some contribution from duricrust. Below this several-millimeter-thick layer exists a matrix of fine sand (150 μm) and smaller-sized particles with only minor contribution from the larger, hematite-bearing spherules. The theoretical thermal inertia derived from such a surface is in the range of 175–300 and is in concordance with the remotely sensed values from orbit as well as those from the rover itself [*Golombek et al.*, 2005; *Fergason and Christensen*, 2005]. Beyond the Opportunity landing area, many geologic features are clear in THEMIS IR images, including >10 layers subjacent to the hematite unit that outcrop along the margins. These layers have contrasting albedos, thermal inertias, and erosional characteristics. The many alternating laminar layers with differing thermophysical and erosional properties suggest periodic deposition of facies with different sedimentary compositions possibly related to clast size, grain orientation and packing, or mineralogy.

7. Landing Sites as Ground Truth

[75] The present analysis provides global and regional context for the measurements made by the MER Spirit and Opportunity rovers. The detailed analysis of the properties of these sites allows us to understand the processes that are responsible for the formation and evolution of the Martian surface layer and to extrapolate these processes to other sites. In addition, we now have five sites on the Martian surface for which we have both remote-sensing data and in situ ground truth. We can use these as a way of understanding the properties that affect and determine thermal inertia, and then use these sites as a guide to help us interpret remote-sensing information for other sites. Figure 14 shows the five landing sites, arranged in order of increasing thermal inertia.

[76] The Spirit and Opportunity sites appear to have the same types of materials that were seen at the earlier three landing sites. All five landing sites show only a few different types of materials. These include fine dust that has been deposited from the atmosphere (shown most clearly as bright red dust sitting on top of rocks or on top of other surface materials at several of the landing sites); windblown material that appears to be loose and unconsolidated and which may have been deposited either as air fall material from the atmosphere or by saltation or traction over the surface (forming structures with shapes indicative of having been moved by the wind); indurated materials suggestive of cemented grains or duricrust; and rocks of different sizes, apparent porosities, and degrees of alteration. Some of the landing sites show morphologies and textures at the surface that appear to have been produced by the same processes that are responsible for the bedrock geology (e.g., the large-scale ripples and possible imbrication at the MPF site, and less so the possible lava-flow morphologies at VL-1 and impact ejecta at VL-2). However, for the discussion here we will focus primarily on the physical properties of the different types of materials that are present at the surface.

[77] In increasing order, the thermal inertias of the vicinities of each of the landing sites are MER-B Opportunity, 220; VL-2, 230; VL-1, 280; MER-A Spirit, 300; and MPF, 390. These values span a range of almost a factor of 1.8 in

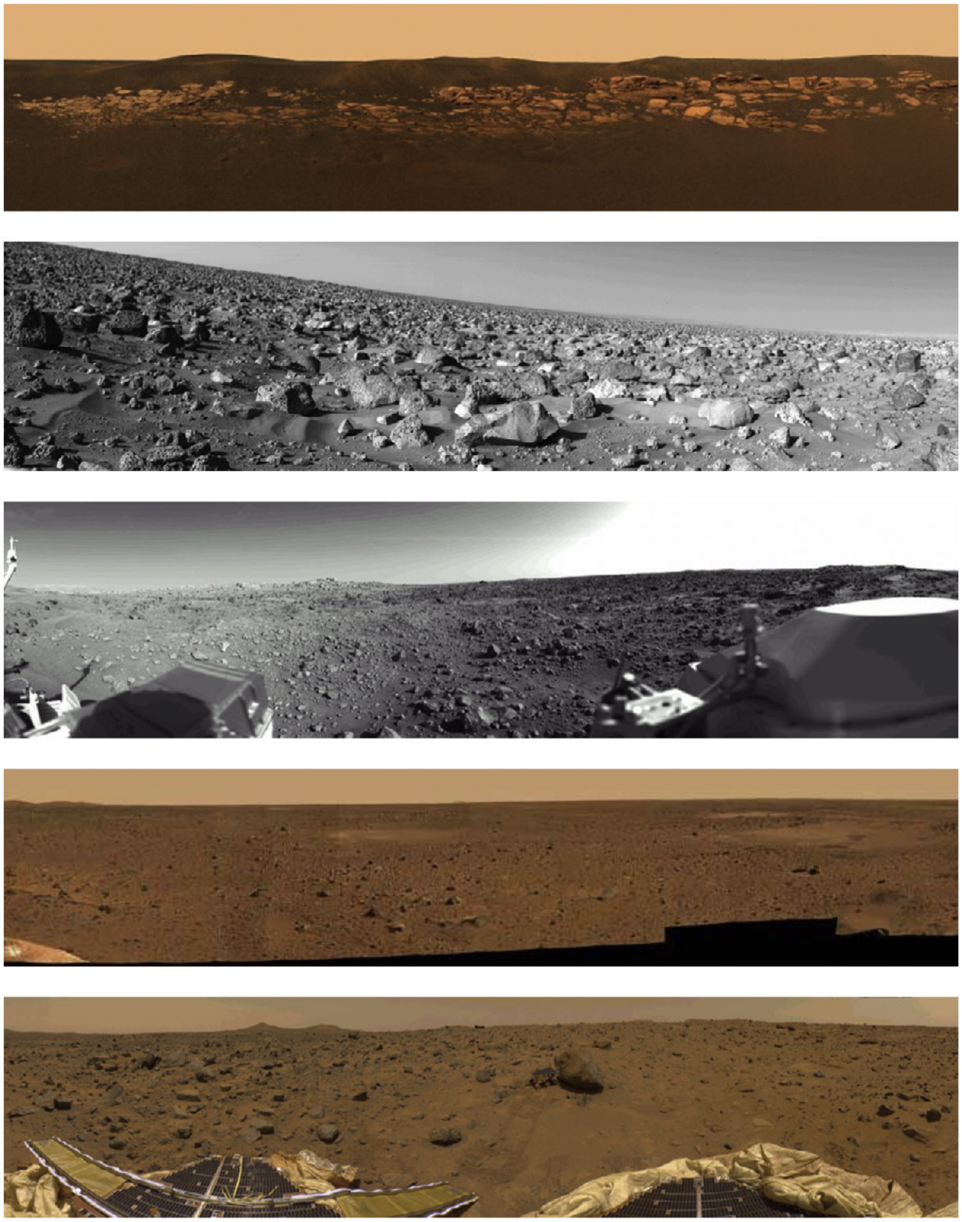

Figure 14. Panorama views of each of the five successful landing sites, shown in order of increasing thermal inertia. Thermal inertias derived from orbiter data are MER-B Opportunity, 220; VL-2, 230; VL-1, 280; MER-A Spirit, 300; MPF, 390.

thermal inertia, equivalent to a factor of 3.1 in the product of thermal conductivity, density, and specific heat (with most of the variability typically being ascribed to the conductivity [see *Kieffer et al.* [1973]). For comparison, global thermal inertias span a total range of from less than 40 to more than 800; this is a factor of 20 in thermal inertia, or a factor of 400 in the product of the component properties. Clearly, the landing sites cover only a limited portion of the total range in thermal properties. Any conclusions about what properties control thermal inertia and about the interpretation of remote-sensing data have to keep this limited range in mind.

[78] Figure 14 shows clearly that the abundance of rocks at the landing sites is not the primary factor determining thermal inertia. The rockiest site (VL-2), in fact, has one of the lowest thermal inertias, and the range in rock abundances between the sites cannot explain the variations in thermal inertia; more explicitly, there is no strong connection between rock abundance and thermal inertia. On the basis of numerical models of the contribution of rocks to the total thermal inertia [e.g., *Golombek et al.*, 2003a], none of the sites has sufficiently abundant rocks to control the thermal inertia, and it must be the properties of the non-rocky component of the surface that dominate.

[79] While fine-grained material is present at each landing site, none of the sites consist predominantly of deposits of loose, unconsolidated grains. This is consistent with the fact that each of the landing sites falls primarily within a mode of thermal inertia and albedo interpreted as consisting of

cemented crusts and some uncemented coarse grains (see Figure 2 and unit C of *Mellon et al.* [2000] and *Putzig et al.* [2005]). This interpretation appears to be confirmed by the in situ observations from the landers and by orbital observations of the absence of dune forms for regions exhibiting sand-like thermal inertias and of the color differences when compared with surfaces composed of unconsolidated materials (see discussion by and references of *Mellon et al.* [2000]).

[80] The major factor that appears to differ significantly between the five surfaces and that is capable of having a large effect on thermal inertia appears to be the properties of the indurated or cemented materials. Individual components that were identified at the different sites were described by their cohesiveness or strength and their friction angles [e.g., *Moore et al.*, 1987, 1999; *Moore and Jakosky*, 1989]. The range goes from materials that appear to be very lightly cemented to very dense crusts. The former are very friable and were able to be disintegrated with ease upon shaking (as seen, for example, at the Viking sites when the landers attempted to sample rocks). It also forms only a very thin layer at the surface in some instances (e.g., in some locations at the MER-B Opportunity site, where crusts occur that are only millimeters thick). The denser crusts are able to support the weight of a spacecraft without losing their integrity (at VL-1) and to resist abrasion by the Sojourner wheels (at the MPF site), but still can be broken apart readily with the grinder on the Opportunity Rock Abrasion Tool [e.g., *Squyres et al.*, 2004b].

[81] The description of the crusts accurately reflects their properties: crusty, cloddy, and blocky [*Moore et al.*, 1987]. The detailed analysis that would allow us to compare the properties of crusts, including the two MER sites, has not yet been done. Having this information would allow us to relate the physical properties of the crusts and their abundances at each site to the overall thermal inertia. As it is the properties of the crust that appear to dominate the overall character of the landing sites, the absence of a quantitative understanding of the crust properties and what controls them is limiting our ability to understand the landing sites and the global properties.

[82] In addition, we have not yet sampled in situ the lowest thermal-inertia values that are likely to consist predominantly of fine-grained material deposited out of the atmosphere. Neither have we sampled the highest values; these have a thermal inertia that is more than a factor of two greater than at the MPF site, and are likely to represent a fundamentally different type of surface material or surface morphology.

[83] We anticipate that the ongoing rover traverses of Spirit and Opportunity will provide additional opportunities to do this type of comparison, in that they are traversing over a number of different terrain types. We can use these analyses to better understand the global processes that affect the surface layer, and detailed studies at these and other sites using multiple remote-sensing data sets will provide key insights into understanding the Martian surface.

[84] **Acknowledgments.** This research was supported in part by the Mars Global Surveyor and Mars Odyssey projects, the Mars Data Analysis Program, the JPL Critical Data Products Program, and the NASA Planetary Geology and Geophysics Program. Valuable comments and assistance were received from Robin Fergason, and helpful reviews were received from Jeff Plescia and Nathan Bridges.

References

Arvidson, R. E., F. P. Seelos IV, K. S. Deal, W. C. Koeppen, N. O. Snider, J. M. Kieniewicz, B. M. Hynek, M. T. Mellon, and J. B. Garvin (2003), Mantled and exhumed terrains in Terra Meridiani, Mars, *J. Geophys. Res.*, *108*(E12), 8073, doi:10.1029/2002JE001982.

Arvidson, R. E., et al. (2004a), Localization and physical properties experiments conducted by Spirit at Gusev Crater, *Science*, *305*, 821–824.

Arvidson, R. E., et al. (2004b), Localization and physical property experiments conducted by Opportunity at Meridiani Planum, *Science*, *306*, 1730–1733.

Binder, A. B., R. E. Arvidson, E. A. Guinness, K. L. Jones, E. C. Morris, T. A. Mutch, D. C. Pieri, and C. Sagan (1977), The geology of the Viking Lander 1 site, *J. Geophys. Res.*, *82*, 4439–4451.

Bridges, J. C., et al. (2003), Selection of the landing site in Isidis Planitia of Mars probe Beagle 2, *J. Geophys. Res.*, *108*(E1), 5001, doi:10.1029/2001JE001820.

Cabrol, N. A., and E. A. Grin (2000), Possible frost mounds in an ancient Martian lake bed, *Icarus*, *145*, 91–107.

Cabrol, N. A., E. A. Grin, A. Dollfus, and G. Dawidowicz (1993), An ancient inner lake in Ma'adim Vallis, *Lunar Planet. Sci.*, *XXIV*, 241–242.

Cabrol, N. A., E. A. Grin, R. Landheim, R. O. Kuzmin, and R. Greeley (1998), Duration of the Ma'adim Vallis/Gusev Crater hydrogeologic system, Mars, *Icarus*, *133*, 98–108.

Christensen, P. R. (1986), The spatial distribution of rocks on Mars, *Icarus*, *68*, 217–238.

Christensen, P. R., and H. J. Moore (1992), The Martian surface layer, in *Mars*, edited by H. H. Kieffer et al., pp. 686–729, Univ. of Ariz. Press, Tucson.

Christensen, P. R., and S. W. Ruff (2004), Formation of the hematite-bearing unit in Meridiani Planum: Evidence for deposition in standing water, *J. Geophys. Res.*, *109*, E08003, doi:10.1029/2003JE002233.

Christensen, P. R., et al. (2000), Detection of crystalline hematite mineralization on Mars by the Thermal Emission Spectrometer: Evidence for near-surface water, *J. Geophys. Res.*, *105*, 9623–9642.

Christensen, P. R., R. V. Morris, M. D. Lane, J. L. Bandfield, and M. C. Malin (2001), Global mapping of Martian hematite mineral deposits: Remnants of water-driven processes on early Mars, *J. Geophys. Res.*, *106*, 23,873–23,886.

Christensen, P. R., et al. (2003), Morphology and composition of the surface of Mars: Mars Odyssey THEMIS results, *Science*, *300*, 2056–2061.

Christensen, P. R., et al. (2004a), The Thermal Emission Imaging System (THEMIS) for the Mars 2001 Odyssey mission, *Space Sci. Rev.*, *110*, 85–130.

Christensen, P. R., et al. (2004b), Initial results from the Mini-TES experiment in Gusev Crater from the Spirit Rover, *Science*, *305*, 837–842.

Christensen, P. R., et al. (2005), Mars Exploration Rover candidate landing sites as viewed by THEMIS, *Icarus*, *176*, 12–43.

Crumpler, L. S., and K. L. Tanaka (2003), Geology and MER target site characteristics along the southern rim of Isidis Planitia, Mars, *J. Geophys. Res.*, *108*(E12), 8080, doi:10.1029/2002JE002040.

Edgett, K. S. (2002), Low-albedo surfaces and eolian sediment: Mars Orbiter Camera views of western Arabia Terra craters and wind streaks, *J. Geophys. Res.*, *107*(E6), 5038, doi:10.1029/2001JE001587.

Edgett, K. S., and M. C. Malin (2002), Martian sedimentary rock stratigraphy: Outcrops and interbedded craters of northwest Sinus Meridiani and southwest Arabia Terra, *Geophys. Res. Lett.*, *29*(24), 2179, doi:10.1029/2002GL016515.

Fergason, R. L., and P. R. Christensen (2005), Thermophysics at the MER Spirit and Opportunity landing sites: Perspectives from the surface and from orbit, *Lunar Planet. Sci.*, *XXXVI*, abstract 1265.

Golombek, M. P., A. F. C. Haldemann, N. K. Forsberg-Taylor, E. N. DiMaggio, R. D. Schroeder, B. M. Jakosky, M. T. Mellon, and J. R. Matijevic (2003a), Rock size-frequency distributions on Mars and implications for Mars Exploration Rover landing safety and operations, *J. Geophys. Res.*, *108*(E12), 8086, doi:10.1029/2002JE002035.

Golombek, M. P., et al. (2003b), Selection of the Mars Exploration Rover landing sites, *J. Geophys. Res.*, *108*(E12), 8072, doi:10.1029/2003JE002074.

Golombek, M. P., et al. (2005), Assessment of Mars Exploration Rover landing site predictions, *Nature*, *436*, 44–48.

Grant, J. A., et al. (2004), Surficial deposits at Gusev Crater along Spirit Rover traverses, *Science*, *305*, 807–810.

Greeley, R., and J. E. Guest (1987), Geologic map of the eastern equatorial region of Mars, 1:15000000, *U.S. Geol. Surv. Misc. Invest. Ser., Map I-1802-B*.

Greeley, R., and S. D. Thompson (2003), Mars: Aeolian features and wind predictions at the Terra Meridiani and Isidis Planitia potential Mars Exploration Rover landing sites, *J. Geophys. Res.*, *108*(E12), 8093, doi:10.1029/2003JE002110.

Greeley, R., M. Kraft, R. Sullivan, G. Wilson, N. Bridges, K. Herkenhoff, R. O. Kuzmin, M. Malin, and W. Ward (1999), Aeolian features and processes at the Mars Pathfinder landing site, *J. Geophys. Res.*, *104*, 8573–8584.

Greeley, R., et al. (2004), Wind-related processes detected by the Spirit Rover at Gusev Crater, Mars, *Science*, *305*, 810–821.

Grin, E. A., and N. A. Cabrol (1997), Limnologic analysis of Gusev crater paleolake, Mars, *Icarus*, *130*, 461–474.

Grizzaffi, P., and P. H. Schultz (1989), Isidis Basin: Site of ancient volatile-rich debris layer, *Icarus*, *77*, 358–381.

Head, J. W., III, M. A. Kreslavsky, and S. Pratt (2002), Northern lowlands of Mars: Evidence for widespread volcanic flooding and tectonic deformation in the Hesperian Period, *J. Geophys. Res.*, *107*(E1), 5003, doi:10.1029/2000JE001445.

Herkenhoff, K. E., et al. (2004a), Textures of the soils and rocks at Gusev Crater from Spirit's Microscopic Imager, *Science*, *305*, 824–826.

Herkenhoff, K. E., et al. (2004b), Evidence from Opportunity's Microscopic Imager for water on Meridiani Planum, *Science*, *306*, 1727–1730, doi:10.1126/science.1105286.

Hiesinger, H., and J. W. Head (2004), The Isidis Basin of Mars: New results from MOLA, MOC, and THEMIS, *Lunar Planet. Sci.*, *XXXV*, abstract 1167.

Hynek, B. M. (2004), Extensive bedrock throughout Terra Meridiani, Mars: Implications for hydrologic processes, *Nature*, *431*, doi:10.1038/nature02902.

Hynek, B. M., and R. J. Phillips (2001), Evidence for extensive denudation of the Martian highlands, *Geology*, *29*, 407–410.

Hynek, B. M., R. E. Arvidson, and R. J. Phillips (2002), Geologic setting and origin of Terra Meridiani hematite deposit on Mars, *J. Geophys. Res.*, *107*(E10), 5088, doi:10.1029/2002JE001891.

Irwin, R. P., T. A. Maxwell, A. D. Howard, R. A. Craddock, and D. W. Leverington (2002), A large paleolake basin at the head of Ma'adim Vallis, Mars, *Science*, *296*, 2209–2212.

Ivanov, M. A., and J. W. Head III (2003), Syrtis Major and Isidis Basin contact: Morphological and topographic characteristics of Syrtis Major lava flows and material of the Vastitas Borealis Formation, *J. Geophys. Res.*, *108*(E6), 5063, doi:10.1029/2002JE001994.

Jakosky, B. M. (1986), On the thermal properties of Martian fines, *Icarus*, *66*, 117–124.

Jakosky, B. M., and P. R. Christensen (1986), Are the Viking Lander sites representative of the surface of Mars?, *Icarus*, *66*, 125–133.

Jakosky, B. M., and M. T. Mellon (2001), High-resolution thermal-inertia mapping of Mars: Sites of exobiological relevance, *J. Geophys. Res.*, *106*, 23,887–23,907.

Jakosky, B. M., and D. O. Muhleman (1981), A comparison of the thermal and radar properties of Mars, *Icarus*, *45*, 25–38.

Jakosky, B. M., M. T. Mellon, H. H. Kieffer, P. R. Christensen, E. S. Varnes, and S. W. Lee (2000), The thermal inertia of Mars from the Mars Global Surveyor Thermal Emission Spectrometer, *J. Geophys. Res.*, *105*, 9643–9652.

Kieffer, H. H., S. C. Chase Jr., E. Miner, G. Munch, and G. Neugebauer (1973), Preliminary report on infrared radiometric measurements from the Mariner 9 spacecraft, *J. Geophys. Res.*, *78*, 4291–4312.

Kieffer, H. H., T. Z. Martin, A. R. Peterfreund, B. M. Jakosky, E. D. Miner, and F. D. Palluconi (1977), Thermal and albedo mapping of Mars during the Viking primary mission, *J. Geophys. Res.*, *82*, 4249–4291.

Kuzmin, R. O., R. Greeley, R. Landheim, N. A. Cabrol, and J. D. Farmer (2000), Geologic map of the MTM-15182 and MTM-15187 quadrangles, Gusev Crater-Ma'adim Vallis region, Mars, *U.S. Geol. Surv. Geol. Invest. Ser.*, *Map I-2666*.

Malin, M. C., and K. S. Edgett (2001), Mars Global Surveyor Mars Orbiter Camera: Interplanetary Cruise through Primary Mission, *J. Geophys. Res.*, *106*, 23,429–23,570.

Martínez-Alonso, S., B. M. Jakosky, M. T. Mellon, and N. E. Putzig (2005), A volcanic interpretation of Gusev Crater surface materials from thermophysical, spectral, and morphological evidence, *J. Geophys. Res.*, *110*, E01003, doi:10.1029/2004JE002327.

McSween, H., et al. (2004), Preliminary mineralogy and geochemistry results at the MER-A landing site in Gusev, *Lunar Planet. Sci.*, *XXXV*, abstract 2167.

Mellon, M. T., B. M. Jakosky, H. H. Kieffer, and P. R. Christensen (2000), High-resolution thermal-inertia mapping from the Mars Global Surveyor Thermal Emission Spectrometer, *Icarus*, *148*, 437–455.

Milam, K. A., K. R. Stockstill, J. E. Moersch, H. Y. McSween Jr., L. L. Tornabene, A. Ghosh, M. B. Wyatt, and P. R. Christensen (2003), THEMIS characterization of the MER Gusev crater landing site, *J. Geophys. Res.*, *108*(E12), 8078, doi:10.1029/2002JE002023.

Moore, H. J., and B. M. Jakosky (1989), Viking landing sites, remote sensing observations, and physical properties of Martian surface materials, *Icarus*, *81*, 164–184.

Moore, H. J., R. E. Hutton, G. D. Clow, and C. R. Spitzer (1987), The physical properties of the surface materials of the Viking landing sites on Mars, *U.S. Geol. Surv. Prof. Pap.*, *1389*.

Moore, H. J., D. B. Bickler, J. A. Crisp, H. J. Eisen, J. A. Gensler, A. F. C. Haldemann, J. R. Matijevic, L. K. Reid, and F. Pavlics (1999), Soil-like deposits observed by Sojourner, the Pathfinder rover, *J. Geophys. Res.*, *104*, 8729–8746.

Muhleman, D. O. (1972), Microwave emission from the Moon, in *Thermal Characteristics of the Moon*, edited by J. W. Lucas, pp. 51–81, MIT Press, Cambridge, Mass.

Mutch, T. A., R. E. Arvidson, A. B. Binder, E. A. Guinness, and E. C. Morris (1977), The geology of the Viking Lander 2 site, *J. Geophys. Res.*, *82*, 4452–4467.

Palluconi, F. D., and H. H. Kieffer (1981), Thermal inertia mapping of Mars from 60S to 60N, *Icarus*, *45*, 415–426.

Parker, T. J., R. S. Saunders, and D. M. Schneeberger (1989), Transitional morphology in west Deuteronilus Mensae, Mars—Implications for modification of the lowland/upland boundary, *Icarus*, *82*, 111–145.

Parker, T. J., D. S. Gorsline, R. S. Saunders, D. C. Pieri, and D. M. Schneeberger (1993), Coastal geomorphology of the Martian northern plains, *J. Geophys. Res.*, *98*(E6), 11,061–11,078.

Pelkey, S. M., B. M. Jakosky, and M. T. Mellon (2001), Thermal inertia of crater-related wind streaks on Mars, *J. Geophys. Res.*, *106*(E10), 23,909–23,920.

Presley, M. A., and P. R. Christensen (1997), Thermal conductivity measurements of particulate materials: 2. Results, *J. Geophys. Res.*, *102*, 6551–6566.

Putzig, N. E., M. T. Mellon, K. A. Kretke, and R. E. Arvidson (2005), Global thermal inertia and surface properties of Mars from the MGS mapping mission, *Icarus*, *173*, 325–341.

Rafkin, S. C. R., and T. I. Michaels (2003), Meteorological predictions for 2003 Mars Exploration Rover high-priority landing sites, *J. Geophys. Res.*, *108*(E12), 8091, doi:10.1029/2002JE002027.

Robinson, M. S., and P. J. Mouginis-Mark (1993), Chronology, eruption duration, and atmospheric contribution of the Martian volcano Apollinaris Patera, *Icarus*, *104*, 301–323.

Rogers, A. D., J. L. Bandfield, and P. R. Christensen (2003), Global bedrock composition mapping on Mars using TES and THEMIS data, *Lunar Planet. Sci.*, *XXXIV*, abstract 2082.

Schneeberger, D. M. (1989), Episodic channel activity at Ma'adim Vallis, Mars, *Lunar Planet. Sci.*, *XX*, 964–965.

Scott, D. H., and K. L. Tanaka (1982), Ignimbrites of the Amazonian Planitia region on Mars, *J. Geophys. Res.*, *87*, 178–1190.

Scott, D. H., E. C. Morris, and M. N. West (1978), Geologic map of the Aeolis quadrangle of Mars, 1:5000000, *U.S. Geol. Surv. Misc. Invest. Ser.*, *Map I-1111*.

Smith, M. D., J. C. Pearl, B. J. Conrath, and P. R. Christensen (2001), Thermal Emission Spectrometer results: Mars atmospheric thermal structure and aerosol distribution, *J. Geophys. Res.*, *106*, 23,929–23,945.

Soderblom, L. A., et al. (2004), Soils of Eagle Crater and Meridiani Planum at the Opportunity Rover landing site, *Science*, *306*, 1723–1726, doi:10.1126/science.1105127.

Squyres, S. W., et al. (2004a), The Spirit Rover's Athena science investigation at Gusev Crater, Mars, *Science*, *305*, 794–799, doi:10.1126/science.3050794.

Squyres, S. W., et al. (2004b), The Opportunity Rover's Athena science investigation at Meridiani Planum, Mars, *Science*, *306*, 1698–1703, doi:10.1126/science.1106171.

Tanaka, K. L. (1986), The stratigraphy of Mars, *Proc. Lunar Planet. Sci. Conf. 17th*, Part 1, *J. Geophys. Res.*, *91*, suppl., E139–E158.

Tanaka, K. L., T. Joyal, and A. Wenker (2000), The Isidis Plains Unit, Mars: Possible catastrophic origins, tectonic tilting, and sediment loading, *Lunar Planet. Sci.*, *XXXI*, abstract 2023.

Veverka, J., P. Gierasch, and P. Thomas (1981), Wind streaks on Mars: Meteorological control of occurrence and mode of formation, *Icarus*, *45*, 154–166.

P. R. Christensen, Department of Geology, Arizona State University, Tempe, AZ 85287, USA.

B. M. Hynek, B. M. Jakosky, S. Martínez-Alonso, M. T. Mellon, N. Murphy, and N. E. Putzig, Laboratory for Atmospheric and Space Physics, University of Colorado, Campus Box 392, Boulder, CO 80309, USA. (bruce.jakosky@lasp.colorado.edu)

S. M. Pelkey, Department of Geological Sciences, Brown University, Providence, RI 02912, USA.